Materials Today Bio 26 (2024) 101091

Contents lists available at ScienceDirect

Materials Today Bio

journal homepage: www.journals.elsevier.com/materials-today-bio

Oxygen self-sufficient nanodroplet composed of fluorinated polymer for high-efficiently PDT eradicating oral biofilm

Bing Cao [a,b,1], Yingfei Ma [c,d,1], Jian Zhang [e,1], Yanan Wang [f], Yating Wen [a,b], Yun li [a,b], Ruixue Wang [a,b], Donghai Cao [g], Ruiping Zhang [c,*]

[a] Shanxi Bethune Hospital, Shanxi Academy of Medical Sciences, Tongji Shanxi Hospital, Third Hospital of Shanxi Medical University, Taiyuan, 030032, China
[b] Tongji Hospital, Tongji Medical College, Huazhong University of Science and Technology, Wuhan, 430030, China
[c] The Radiology Department of Shanxi Provincial People's Hospital, Five Hospital of Shanxi Medical University, Taiyuan, 030001, China
[d] College of Medical Imaging, Shanxi Medical University, Taiyuan, 030001, China
[e] Key Laboratory of Interface Science and Engineering in Advanced Materials Ministry of Education, Taiyuan University of Technology, Taiyuan, 030024, China
[f] The Department of Physiology, School of Basic Medical Sciences, Shanxi Medical University, Taiyuan, 030001, China
[g] College of Traditional Chinese Medicine and Food Engineering, Shanxi University of Chinese Medicine, Taiyuan, 030024, China

ARTICLE INFO

Keywords:
Oral-biofilm
Dental caries
Nanodroplets
AIE photosensitizer
Fluorinated-polymer

ABSTRACT

Oral biofilm is the leading cause of dental caries, which is difficult to completely eradicate because of the complicated biofilm structure. What's more, the hypoxia environment of biofilm and low water-solubility of conventional photosensitizers severely restrict the therapeutic effect of photodynamic therapy (PDT) for biofilm. Although conventional photosensitizers could be loaded in nanocarriers, it has reduced PDT effect because of aggregation-caused quenching (ACQ) phenomenon. In this study, we fabricated an oxygen self-sufficient nanodroplet (PFC/TPA@FNDs), which was composed of fluorinated-polymer (FP), perfluorocarbons (PFC) and an aggregation-induced emission (AIE) photosensitizer (Triphenylamine, TPA), to eradicate oral bacterial biofilm and whiten tooth. Fluorinated-polymer was synthesized by polymerizing (Dimethylamino)ethyl methacrylate, fluorinated monomer and 1-nonanol monomer. The nanodroplets could be protonated and behave strong positive charge under bacterial biofilm acid environment promoting nanodroplets deeply penetrating biofilm. More importantly, the nanodroplets had extremely high PFC and oxygen loading efficacy because of the hydrophobic affinity between fluorinated-polymer and PFC to relieve the hypoxia environment and enhance PDT effect. Additionally, compared with conventional ACQ photosensitizers loaded system, PFC/TPA@FNDs could behave superior PDT effect to ablate oral bacterial biofilm under light irradiation due to the unique AIE effect. *In vivo* caries animal model proved the nanodroplets could reduce dental caries area without damaging tooth structure. *Ex vivo* tooth whitening assay also confirmed the nanodroplets had similar tooth whitening ability compared with commercial tooth whitener H_2O_2, while did not disrupt the surface microstructure of tooth. This oxygen self-sufficient nanodroplet provides an alternative visual angle for oral biofilm eradication in biomedicine.

1. Introduction

Bacterial infection is a major cause for human diseases, most of which are related with bacteria biofilm [1]. Dental caries is a typical disease caused by oral biofilm, threatening human health. In the oral environment, sugar-rich diet provides bacteria with abundant nutrition conditions, and once under poor oral hygiene bacteria immediately grow and adhere to tooth, and form bacterial biofilm, disrupting tooth and causing many oral diseases [2]. In biofilm, microbes are encapsulated by extracellular polymeric substances (EPS) which are mainly composed of polysaccharides, proteins, lipids and extracellular DNA [3]. The EPS not only provide microenvironment for microbial growth, but also protect bacteria from threatening challenges, which makes it a thorny problem [4]. Recent data evaluated by Global Burden of Disease demonstrated untreated dental caries occurred globally 30,129 cases per 100, 000, and caused $ 22.09 billion indirect cost per year globally [5,

* Corresponding author. The Radiology Department of Shanxi Provincial People's Hospital, The Fifth Hospital of Shanxi Medical University, 29 Shuangta East Street, Taiyuan, 030001, China.
E-mail address: zrp_7142@sxmu.edu.cn (R. Zhang).
[1] The authors have contributed equally.

https://doi.org/10.1016/j.mtbio.2024.101091
Received 15 February 2024; Received in revised form 12 May 2024; Accepted 14 May 2024
Available online 15 May 2024

6]. Topically applied drug was a main option for treating oral bacterial biofilm, but it suffered from rapid salivary clearance, poor penetration of biofilm, some adverse effects and so on, leading to limited biofilm eradication efficiency [7]. Therefore, it is imperative to develop new oral antibiofilm strategies to combat biofilm-related cariogenic challenges.

Photodynamic therapy (PDT) is a noninvasive treatment technique which has been widely used in anticancer and antibacterial fields [8–10]. PDT involves three key elements: oxygen, photosensitizer (PS) and light. After illuminating PS with light of a specific wavelength, the excited PS could transfer energy to molecular oxygen and generate cytotoxic reactive oxygen species (ROS) [11,12]. PDT has also been used in oral biofilm field, for example, a bifunctional zwitterion-modified porphyrin [13], curcumin [14], and rose bengal [15]. Oxygen plays an important role in PDT, but oxygen is consumed faster than the rate of diffusion in biofilm, resulting in anaerobic zones deep in the biofilm [4]. As a result, conventional PDT could not eradicate biofilm completely. Some oxygen self-sufficient strategies have been developed to enhance PDT efficacy. As artificial blood substitutes, perfluorocarbons (PFC) has high oxygen solubility and is a commonly used oxygen carrier for enhancing PDT efficiency [16,17]. Oxygen self-sufficient strategies also have been used in oral biofilm, such as MnO_2 catalysis for oxygen or delivery of oxygen [18,19]. Although the therapeutic effects are pretty good, the efficacy can still be promoted. Ce6 and BODIPY-I are classical aggregation-caused quenching (ACQ) photosensitizers, which have low fluorescence signals and photosensitive efficiency when they are encapsulated in nanocarriers with high concentrations or aggregate states [20]. On the contrary, aggregation-induced emission (AIE) photosensitizer is a new type of photosensitizer, which is emissive in aggregate state via restriction of intramolecular motions and shows improved ROS production in the aggregate state [21–23]. As the typical class of AIE photosensitizer [24], triphenylamine (TPA) often have good PDT efficiency under short-wavelength light irradiation, and could match the clinical curing light (420–480 nm). So, incorporating oxygen self-sufficient strategies and AIE photosensitizer to develop a new PDT system would have great potential for oral biofilm ablation by the extremely enhanced PDT efficacy.

Additionally, penetration in biofilm is the prerequisite for better behaving antibiofilm ability. But EPS extremely restrict the penetration of antibiotic. It has been reported that nanoparticles with size <350 nm and without charge or cationic charge could penetrate biofilms, cationic nanoparticles have better distribution throughout the matrix [25]. In our previous work, we have proved poly(Dimethylamino)ethyl methacrylate can respond to biofilm acid environment to be protonated, and have enhanced positive charge, which promote nanoparticles to deeply penetrate biofilm [26]. The pH in oral biofilm could reach 4.5–5.5 [27]. Designing cationic nanoparticles with pH-responsive function could avoid probable side effects in circulation [28]. Hence, it is rational to develop antibiofilm system adopting pH-responsive strategy according to the acid environment of oral biofilm.

In the present work, we synthesized a fluorinated-polymer (FP) with pH-responsive cationic charge enhanced ability, by polymerizing (Dimethylamino)ethyl methacrylate (DMAEMA), fluorinated monomer (FMA) and 1-nonanol monomer (NMA). And then FPs loaded PFC and AIE photosensitizers (TPA) fabricating a kind of nanodroplet (PFC/TPA@FNDs) by using emulsion method (Scheme. 1a). PFC/TPA@FNDs have pretty high PFC loading efficacy because of the F–F hydrophobic affinity, and as a result PFC/TPA@FNDs can load much higher oxygen to formed O_2@PFC/TPA@FNDs. More importantly, the AIE photosensitizer-TPA in nanodroplets has strong fluorescence and high photosensitive efficiency because of the unique AIE phenomenon when in aggregation state. When applied in oral biofilm, O_2@PFC/TPA@FNDs could be protonated with the strong positive charge under acid biofilm environment, promoting nanodroplets deep penetration. Subsequently, O_2@PFC/TPA@FNDs relieve biofilm hypoxia condition and behave highly effective PDT to eradicate oral biofilm upon light irradiation (Scheme. 1b). What's more, like commercial peroxides tooth whitener, O_2@PFC/TPA@FNDs also have good tooth whitening ability, but would

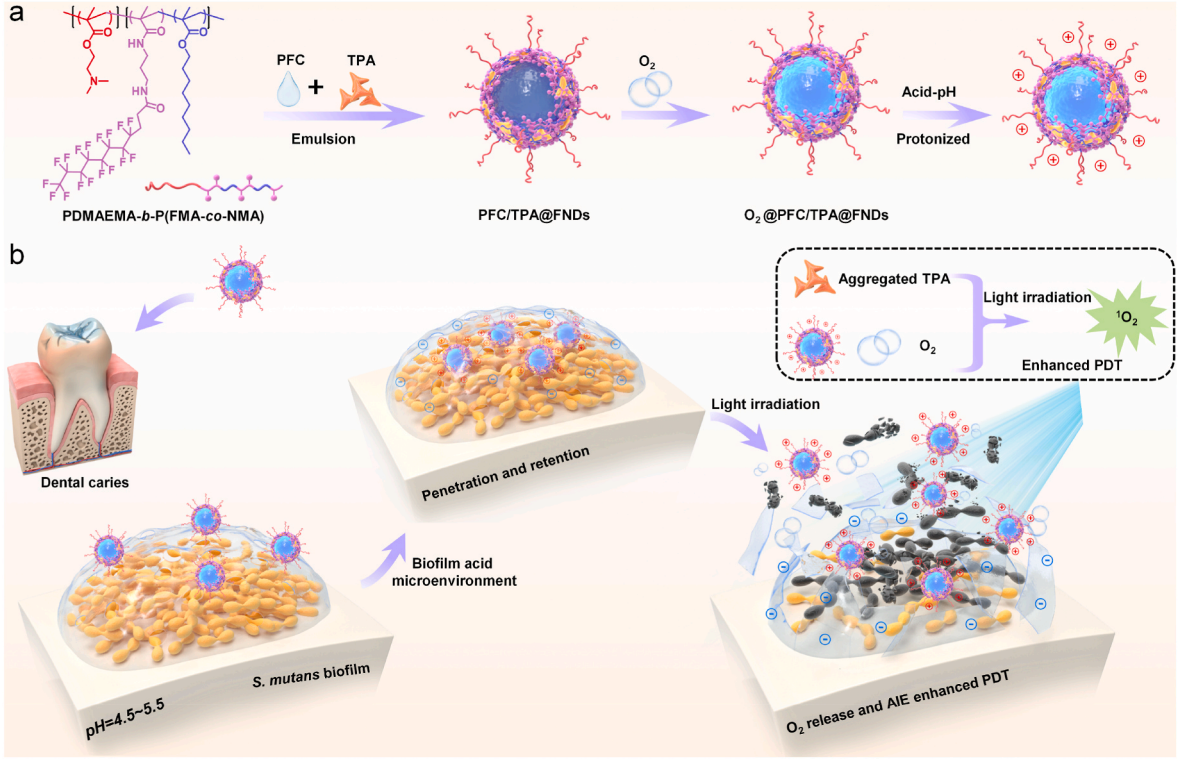

Scheme 1. (a) Schematic illustration for the design of oxygen self-sufficient nanodroplet composed of fluorinated polymer (PDMAEMA-*b*-P(FMA-*co*-NMA)), perfluorocarbons (PFC) and AIE photosensitizer-TPA. (b) Therapeutic application of nanodroplet for animal dental caries model.

not disrupt the microstructure of tooth surface. Animal dental caries model also proved the good therapeutic ability of nanodroplets, which is a potential candidate for the future clinical oral-biofilm treatment.

2. Materials and methods

2.1. Materials

N-(3-Aminopropyl) methacrylamide hydrochloride (APMA), 2-aminotoluene-5-sulfonic acid, 1-nonanol, perfluorooctyl bromide (PFC), bis(pinacolato)diboron, (4-bromo-*N, N*-bis(4-Methoxyphenyl)aniline), potassium acetate, potassium carbonate, and 9,10-anthracenediyl-bis (methylene) dimalonic acid (ABDA) were purchased from Macklin Biochemical Co., Ltd (Shanghai, China). 1,3,5-trimethoxybenzene was purchased from Alfa Aesar (China)Chemical Co., Ltd. Triethylamine was purchased from Xiya Reagent. O-benzotriazol-1-yl-tetramethyluronium hexafluorophosphate (HBTU), 2,2′-Azobis(2-methylpropionitrile), and 2-(Dimethylamino)ethyl methacrylate, 2,2,6,6-Tetramethyl-4-piperidone (TEMP) were purchased from Aladdin Biochemical Technology Co., Ltd (Shanghai, China). [1,1′-Bis(diphenylphosphino) ferrocene] dichloropalladium(II) and methacryloylchloride were purchased from Energy Chemical. 4-cyano-4-(thiobenzoylthio) pentanoic acid, tetrakis (triphenylphosphine)palladium, and 4-bromo-2,1,3-benzothiadiazole were purchased from Bide Pharmatech Ltd. Polyvinyl alcohol (PVA) was purchased from Sigma-Aldrich (Shanghai) Trading Co., Ltd. Dimethyl sulfoxide (DMSO) and N, N-Dimethylformamide (DMF) were purchased from Tianjin Jindong Tianzheng Fine Chemical Reagent Factory. Dichloromethane, petroleum ether, tetrahydrofuran, ethyl acetate, sodium sulfate anhydrous (Na_2SO_4), and sucrose were obtained from Tianjin Beichen District Fangzheng Reagent Factory; 1,4-dioxane was obtained from Rhawn reagent (Shanghai, China). SYTO 9 was purchased from Thermo Fisher Scientific; propidium iodide (PI) staining solution and Cell Counting Kit (CCK-8) were purchased from Yeasen Biotechnology (Shanghai) Co., Ltd. BCA Protein Assay Kit was purchased from Beyotime Biotechnology. Brain Heart Infusion Broth (BHI) was purchased from Guangdong Huankai Bio Technology Co., Ltd. *Streptococcus mutans* (*S. mutans*, ATCC 25175) was used as a representative bacterium to form biofilm model and purchased from China General Microbiological Culture Collection Center (CGMCC). All reagents and chemicals are used without further purification unless otherwise stated. Water used in this was deionized with a Milli-Q reagent water system.

2.2. Synthesis of fluorinated monomer (FMA)

Firstly, N-(3-Aminopropyl) methacrylamide hydrochloride (APMA, 0.164 g, 0.896 mmol) and triethylamine (0.16 mL, 2.33 mmol) were dissolved in 2 mL DMF into a glass ampoule, and stirred at room temperature for 30 min. Subsequently, 2-aminotoluene-5-sulfonic acid (0.44 g, 0.894 mmol), HBTU (1.2 g, 3.164 mmol) and DMF (2 mL) were charged into above ampoule and stirred at room temperature for 3 d. The mixture was diluted with ethyl acetate and respectively washed five times with water and brine. The organic layer was dried with anhydrous Na_2SO_4, and evaporated by a rotary evaporator. Finally, the residue was purified by silica gel column chromatography using petroleum ether/ethyl acetate (1/9 v/v) as the eluent, obtaining FMA as a light brown solid (0.37 g, yield:61.26 %) which was confirmed by detailed ^{1}H NMR analysis.

2.3. Synthesis of 1-nonanol monomer (NMA)

NMA was synthesized by esterification of 1-nonanol with methacryloylchloride. Typically, 1-nonanol (1.2 mL, 6.93 mmol), triethylamine (1.95 mL, 13.835 mmol), and dry DCM (20 mL) were charged into a 100 mL round-bottom flask, cooled to 0 °C in ice water, then methacryloylchloride (0.81 mL, 8.322 mmol) in 20 mL dry DCM was added dropwise for 2 h under vigorous magnetic stirring, then the reaction mixture was stirred at room temperature for 24 h. The solution was diluted with DCM and washed five times with water and brine. The organic layer was dried with anhydrous Na_2SO_4, and evaporated by the rotary evaporator. Finally, the residue was purified by silica gel column chromatography using petroleum ether/DCM (9/1 v/v) as the eluent, obtaining NMA as a transparent viscous liquid (0.75 g, yield:40.11 %) which was confirmed by detailed ^{1}H NMR analysis.

2.4. Synthesis of TPA

4-bromo-N, N-bis(4-Methoxyphenyl) aniline (3 g, 7.8 mmol), bis (pinacolato)diboron (5 g, 19.69 mmol), potassium acetate (3.4 g, 34.69 mmol), [1,1′-Bis(diphenylphosphino) ferrocene] dichloropalladium(II) (200 mg, 0.27 mmol) and 1,4-dioxane (70 mL) were charged into 250 mL round-bottom flask. The flask was degassed via three freeze-pump-thaw cycles. And heated to reflux for 48 h under a nitrogen atmosphere. After cooling to room temperature, the reaction mixtures were extracted with DCM and washed five times with deionized water. The organic layer was dried with anhydrous Na_2SO_4, and evaporated by the rotary evaporator. Finally, the residue was purified by silica gel column chromatography using petroleum ether/dichloromethane (3/1 v/v) as the eluent, obtaining TPA-B as a white oil liquid (1.5 g, yield:19.38 %) which was confirmed by detailed ^{1}H NMR analysis. Subsequently, a 100 mL round-bottom flask was charged with TPA-B (1.55 g, 3.6 mmol), 4-bromo-2,1,3-benzothiadiazole (0.605 g, 2.81 mmol), potassium carbonate (6 g, 43.48 mmol), tetrakis(triphenylphosphine)palladium (0.26 g, 0.225 mmol), methylbenzene (15 mL), deionized water (10 mL), and THF (10 mL). It was performed using a similar procedure as described for TPA-B, obtaining TPA as an orange solid (0.8 g, yield:37.12 %). Finally, TPA was characterized by ^{1}H NMR analysis.

2.5. Synthesis of PDMAEMA

Polymers were obtained through the reversible addition-fragmentation chain transfer (RAFT) polymerization technique. Typically, chain transfer agent, 4-cyano-4-(thiobenzoylthio) pentanoic acid (CTA, 104 mg, 0.372 mmol), 2-(Dimethylamino)ethyl methacrylate (DMAEMA, 1730 mg, 11 mmol) and 2,2′-Azobis(2-methylpropionitrile) (AIBN, 12.28 mg, 0.074 mmol) were dissolved in 1,4-dioxane (2 mL) into a glass ampoule. The ampoule was degassed via three freeze-pump-thaw cycles and flame-sealed under vacuum. It was then immersed into an oil bath thermostated at 70 °C to start the polymerization. After 24 h, the polymerization was quenched into liquid nitrogen to terminate it. The mixtures were precipitated into an excess of petroleum ether to generate red residues, the residues were dissolved in DCM and precipitated into petroleum ether. After three cycles of dissolution-precipitation, the final product was dried in a vacuum oven overnight at room temperature yielding a red solid (1005 mg, yield:55 %). The degree of polymerization of DMAEMA was determined to be 44 based on the ^{1}H NMR analysis.

2.6. Synthesis of PDMAEMA-b-P(FMA-co-NMA)

$PDMAEMA_{44}$ was further employed as a macro-RAFT agent for the polymerization of FMA and RNA. Typically, $PDMAEMA_{44}$ (330 mg, 0.041 mmol), FMA (660 mg, 1.07 mmol), NMA (107.2 mg, 0.505 mmol), and AIBN (1.67 mg, 0.010 mmol) were charged into a glass ampoule containing 2.75 mL 1,4-dioxane and dimethyl sulfoxide (DMSO) mixed solvents (8:3, v/v). It was performed using a similar procedure as described for $PDMAEMA_{44}$. The solution was precipitated into an excess of methyl *tert*-butyl ether to generate red residues, the residues were dissolved in DCM and precipitated into petroleum ether. After three cycles of dissolution-precipitation, the final product was dried in a vacuum oven overnight at room temperature yielding a red solid (450 mg, yield:58.66 %). The degree of polymerization of P(FMA-*co*-NMA)

was determined to $PDMAEMA_{44}$-*b*-P(FMA_9-*co*-NMA_{16}) based on the ^1H NMR analysis. In addition, PDMAEMA-*b*-PNMA was prepared according to similar procedures, and the degree of polymerization of NMA was determined to $PDMAEMA_{44}$-*b*-$PNMA_{22}$ based on the ^1H NMR.

2.7. Preparation of PFC/TPA@FNDs

PFC/TPA@FNDs were fabricated via a modified two-stop emulsion process [26]. Typically, $PDMAEMA_{44}$-*b*-P(FMA_9-*co*-NMA_{16}), TPA and perfluorooctyl bromide (PFC) were added in DCM, then the dispersion was emulsified with an ultrasonic probe at 900 W for 11 min in an ice bath (period of 3 s with the interval of 4 s). After that, a slight amount of PVA aqueous solution was added to the emulsion and further ultrasonicated in the ice bath in an identical condition. Next, DCM was removed from the emulsion by using the rotary evaporator. Finally, the emulsion dispersion was dialyzed against deionized water (Mw cutoff = 3.5 kDa) to remove free TPA. The nanodroplets were stored in a centrifuge tube at 4 °C for further use. In addition, PFC/TPA@MNDs was fabricated using a similar method by replacing $PDMAEMA_{44}$-*b*-P(FMA_9-*co*-NMA_{16}) with $PDMAEMA_{44}$-*b*-$PNMA_{22}$.

2.8. Characterizations

The morphology of the prepared samples was characterized under a transmission electron microscope (TEM, JEM-2100F, JEOL Japan) operated at an accelerating voltage of 80 kV or 200 kV and scanning electron microscopy (SEM Carl Zeiss AG Gemini 300). The hydrodynamic diameters of the PFC/TPA@FNDs were measured by dynamic light scattering (DLS, NANO ZS90, U.K). To analyze the pH-dependent changes of nanodroplets' surface charges, the test samples were dispersed in disodium hydrogen phosphate-citrate buffer (pH 4.4, 5.6, 7.4 or 8) and their Zeta-potentials were detected by Zetasizer (NANO ZS90, U.K). The UV–visible spectra of the PFC/TPA@FNDs, TPA and FNPs were recorded using a UV–Vis spectrometer (UV-6100). All nuclear magnetic resonance (NMR) spectra were recorded on a Bruker AVANCE III 400 MHz NMR spectrometer. The photoluminescence of TPA and PFC/TPA@FNDs were measured by steady state and transient state fluorescence spectrometer (FLS 1000, Edinburgh, UK). Confocal laser scanning microscopy (CLSM) images were obtained using FLUOVIEW FV3000. The loading capacity of PFC in PFC/TPA@FNDs was measured by gas chromatography spectrometry (GC, Huifen, GC-7820, Shanghai). The oxygen loading capacity of PFC/TPA@FNDs was evaluated by the portable dissolved oxygen meter (Rex, JPBJ-608, China).

2.9. Measurement of PFC loading amount for PFC/TPA@FNDs

The loading capacity of PFC in PFC/TPA@FNDs was evaluated by gas chromatography (GC) analysis following the literature protocol with slight modification [29]. PFC/TPA@FNDs (0.8 mg/mL, 50 μL) were dissolved in acetonitrile (100 μL) and vortex-mixed for 2 min. Then, 1,1,1,3,3-pentafluorobutane (200 μL) was added to each sample, and the mixture was vortex-mixed for 5 min. The mixture was centrifuged (1500 g, 2 min, 4 °C) and then frozen at −20 °C overnight. Just before analysis by GC, the lower phase was put into another 1.5 mL tube including 1,3,5-trimethoxybenzene (10 mg). Then, 1 μL of the solution was injected into the chromatograph for GC (Huifen, GC-7820, Shanghai) measurement to determine the concentrations of PFC in each sample. In addition, the pure PFC was treated with the same operation to gain a standard curve. All experiments were performed under 4 °C.

2.10. Evaluation of oxygen loading capacity of PFC/TPA@FNDs

The oxygen loading capacity of PFC/TPA@FNDs nanodroplets was detected by the portable dissolved oxygen meter (Rex, JPBJ-608, China). In brief, PFC/TPA@FNDs (0.2 mg/mL, 3 mL) pretreated with O_2 bubbling were diluted with deionized water pretreated with N_2 bubbling. Then oxygen concentration was measured for 20 min by using a portable dissolved oxygen meter. In addition, PFC/TPA@FNDs solution with N_2, deionized water with O_2, and deionized water with N_2 were treated as control groups [29].

2.11. ROS generating test

As $^1O_2$ was considered the first ROS generated during PDT, 9,10-anthracenediyl-bis(methylene) dimalonic acid (ABDA) was used as the $^1O_2$ indicator [30]. PFC/TPA@FNDs, O_2@PFC/TPA@FNDs (pretreated with O_2 bubbling), and TPA were mixed respectively with the commercial ABDA, then irradiated with an LED blue light (445 nm ± 5 nm, 56 mW/cm^2). After different periods of time irradiation, the ABDA absorbance of each sample was recorded with a UV–Vis spectrometer (UV-6100). To determine the generation of $^1O_2$, electron paramagnetic resonance (EPR) spectrometer was also used. The solution of O_2@PFC/TPA@FNDs (0.2 mL, 0.2 mg/mL) in presence of 2,2,6,6-Tetramethyl-4-Piperidone (TEMP, 0.006 mL) was treated with LED blue light irradiation (445 nm ± 5 nm, 56 mW/cm^2) for 0 min, 3 min, 5 min, followed by detection through EPR spectrometer (EMXPLUS10/12, Bruke).

2.12. Bacterial inhibition analysis

S. mutans (ATCC 25175) is one of the most primary pathogens of caries, which was used as a model in the experiment. Typically, a single colony of *S. mutans* was inoculated in BHI broth at 37 °C, after shaking overnight, the turbid suspension was diluted with BHI broth to OD_{600} = 0.1 and resuspended in BHI to grow until the midlogarithmic phase was reached. The suspension was finally diluted to OD_{600} = 0.001, corresponding to 1 × 10^6 CFU mL^{-1} based on colony counting on BHI agar plates. The bacterial solution (10^6 CFU mL^{-1}, 0.1 mL, pH 4.5 or 7.4) and different concentrations of O_2@PFC/TPA@FNDs (0.1 mL) were inoculated into each well in a 96-well plate and co-cultured at 37 °C for 30 min. Light group: O_2@PFC/TPA@FNDs + bacteria + light, irradiated with blue light (445 ± 5 nm, 56 mW/cm^2, 5 min). Dark group: O_2@PFC/TPA@FNDs + bacteria, without light irradiation. Then, the mixtures were diluted 10^2-fold by PBS, 0.1 mL of the suspensions was plated onto BHI agar plates and incubated for 48 h to count the number of colonies. Meanwhile, the samples were placed on a formvar/carbon-coated 200 mesh copper grid and left to dry at room temperature, and observed the morphologies of bacteria in each group by TEM analysis. In addition, the bacteria in each group were fixed with 2.5 % glutaraldehyde at 4 °C for 4 h, then washed with PBS. The samples were subjected to gradient dehydration in ethanol-water solution with ethanol concentration of 30 %, 50 %, 70 %, 90 %, 95 %, and anhydrous ethanol in turn, and replaced with tert-butanol. Finally, the samples were dried using the freeze dryer, and the morphology of bacteria in each group was evaluated by SEM (Carl Zeiss AG Gemini 300).

2.13. Adhesion of PFC/TPA@FNDs

Bacteria dispersion (10^8 CFU mL^{-1}, 0.1 mL) was respectively incubated with PFC/TPA@FNDs (0.2 mg/mL, 0.1 mL) in disodium hydrogen phosphate-citrate buffer (pH 4.5, 0.2 mL) at 37 °C for 0 min, 5 min, 15 min or 30 min. Subsequently, the resultant mixtures were centrifuged at 4000 rpm for 5 min to remove the supernatant and washed with normal saline (NS) three times. The mixtures were resuspended into SYTO 9 (1.25 μM, 0.3 mL) and incubated at 37 °C at dark for 30 min. Eventually, the stained bacterial cells were imaged by CLSM (FLUOVIEW FV3000, OLYMPUS). Green and pink fluorescence represented bacteria and PFC/TPA@FNDs, respectively. Meanwhile, the mixtures were placed on a formvar/carbon-coated 200 mesh copper grid and left to dry at room temperature, and observed the morphologies of bacteria in each group by TEM (TEM, JEM-2100F, JEOJ, Japan) analysis.

2.14. Bacteria CLSM assays

LIVE/DEAD bacterial viability assay was determined as the following procedure. The mixtures of bacteria dispersion (10^7 CFU mL^{-1}, 1 mL), O_2@PFC/TPA@FNDs (0.2 mg/mL, 0.1 mL) and disodium hydrogen phosphate-citrate buffer (pH 4.5, 0.2 mL) were incubated at 37 °C for 30 min. And then irradiated with blue light (445 ± 5 nm, 56 mW/cm^2, 5 min) or not. Subsequently, the resultant mixtures were centrifuged at 4000 rpm for 5 min to remove the supernatant and washed with normal saline (NS) three times. The mixtures were resuspended into dye solution (0.3 mL), prepared from a mixture of SYTO 9 (485/498 nm, 1.25 μM) and propidium iodide (PI, 535/617 nm, 0.75 μM) in NS, and incubated at 37 °C at dark for 30 min. Eventually, the stained bacterial cells were imaged by CLSM (FLUOVIEW FV3000, OLYMPUS). Bacteria stained with green and red were viable and dead, respectively.

Bacteria DCFH-DA assays were determined as the similar procedure. Bacteria dispersion (10^7 CFU mL^{-1}, 1 mL) was incubated with O_2@PFC/TPA@FNDs or NS for 30 min, then treated DCFH-DA (10 μM, 488/520 nm) for 1 h. After that, bacteria were irradiated with light (445 ± 5 nm, 56 mW/cm^2, 5 min) or not. Subsequently, the resultant mixtures were centrifuged at 4000 rpm for 5 min to remove the supernatant and washed with NS and water. Eventually, the stained bacterial cells were imaged by CLSM (FLUOVIEW FV3000, OLYMPUS).

2.15. Biofilm formation of S. mutans

Typically, *S. mutans* suspension (10^5 CFU mL^{-1}, 0.2 mL) supplemented with BHI broth (containing 2 % sucrose) was inoculate to 96-well microtiter plates, and incubated at 37 °C for 48 h, every 24 h exchanged medium with fresh BHI broth (containing 2 % sucrose). Subsequently, unbound bacteria and medium were removed by washing with PBS buffer under sterile conditions, and the formed biofilm could be seen at the bottom of wells.

2.16. Biofilm penetration assay

S. mutans were cultured to biofilm on a poly(methyl methacrylate) (PMMA) slide (10 mm × 10 mm × 0.2 mm) and placed in 24-well microtiter plates [31], then incubated 37 °C for 48 h. Subsequently, unbound bacteria and medium were removed by washing with NS buffer under sterile conditions. NS and O_2@PFC/TPA@FNDs (0.2 mg/mL, 0.4 mL) were added to the 24-well microtiter plated and incubated for 0 min, 15 min and 30 min, respectively. The PMMA were respectively washed with NS and deionized water five times to remove the redundant sample. The bacterial biofilm images were captured using the CLSM (FLUOVIEW FV3000, OLYMPUS). Green and pink fluorescence represented bacteria and PFC/TPA@FNDs, respectively. The captured images were further processed with commercial Imaris software.

2.17. Biofilm inhibition analysis

The obtained biofilms were incubated with PBS, PFC/TPA@MNDs, O_2@PFC/TPA@MNDs, PFC/TPA@FNDs and O_2@PFC/TPA@FNDs for 30 min. The groups were divided into Control, Light group and Dark group. Control group: biofilms + PBS. Light group: biofilm + sample + blue light (445 ± 5 nm, 56 mW/cm^2) irradiation 5 min. Dark group: biofilm + sample without light irradiation. The residual biofilms were washed with PBS for three times, and harvested by sonication for 5 min. Finally, the CFUs in biofilm were calculated by plating analysis. The groups of no-light were regarded as control.

S. mutans were cultured to biofilms on hydroxyapatite discs (Φ 8 × 2 mm) or teeth. Then unbound bacteria and medium were removed by washing with NS buffer under sterile conditions. The formed biofilms were incubated with PBS and O_2@PFC/TPA@FNDs for 30 min, and irradiated with blue light (445 ± 5 nm, 56 mW/cm^2, 5 min) or not, the groups of no-light were regarded as control. Subsequently, the hydroxyapatite discs or teeth were fixed with 2.5 % glutaraldehyde at 4 °C for 4 h, and washed with PBS. Then the samples were subjected to a graded ethanol dehydration procedure, and replaced with tert-butanol. Finally, the samples were dried using the freeze dryer, and the morphology of bacteria was evaluated via SEM (Carl Zeiss AG Gemini 300).

2.18. Biofilm LIVE/DEAD staining assay

Biofilm cultured at PMMA was washed with NS buffer under sterile conditions to remove the unbound bacteria and the medium. The formed biofilms were incubated with PBS, PFC/TPA@MNDs, O_2@PFC/TPA@MNDs, PFC/TPA@FNDs, and O_2@PFC/TPA@FNDs for 30 min. After blue light (445 ± 5 nm, 56 mW/cm^2, 5 min) irradiation or not, the residual biofilms were washed with NS three times, respectively, and stained by dye solution (0.3 mL) prepared from a mixture of SYTO 9 (1.25 μM) and PI (0.75 μM) in NS, and incubated at 37 °C at dark for 30 min. The groups of no-light were regarded as control. Eventually, 2D and 3D confocal images were obtained on CLSM (FLUOVIEW FV3000, OLYMPUS). Green and red fluorescence represented live and dead bacteria, respectively. The captured images were further processed with commercial Imaris software.

2.19. Biofilm protein production in EPS

The protein amount in biofilm EPS was evaluated by BCA Protein Assay Kit [32]. Typically, *S. mutans* suspension (10^7 CFU mL^{-1}, 0.1 mL) supplemented with BHI broth (containing 2 % sucrose) was inoculate to 96-well microtiter plates, and then added 0.1 mL PBS, O_2@PFC/TPA@FNDs. After incubated at 37 °C for 0.5 h, conducted light irradiation or not. Then, incubated at 37 °C for 48 h. Subsequently, medium was removed by washing with PBS buffer under sterile conditions. Then, used BCA Protein Assay Kit to evaluated protein amount by detect the absorbance in 562 nm.

2.20. Hemolytic activity assay

Potential toxicity against mouse red blood cells (RBCs) was evaluated by a hemoglobin release assay. Fresh blood collected from SD mice was centrifuged at 1500 rpm for 15 min, then the supernatant was removed and the RBCs were washed gently with NS three additional times. Subsequently, the obtained RBCs were diluted with NS, and the diluted RBC solution (0.1 mL) was mixed with PFC/TPA@FNDs (1.1 mL) at different concentrations in a capped centrifuge tube. After incubating at 37 °C for 2 h, each sample was centrifuged at 1500 rpm for 15 min, and the absorbance of the supernatant (0.1 mL) at 540 nm was examined using a microplate reader (Spectra Max Plus384). The NS group and deionized water group were used as negative and positive hemolysis. The hemolysis rate was calculated according to the following formula:

$$\text{Hemolysis ratio (\%)} = (OD_0\text{-}OD_1)/(OD_2\text{-}OD_1) *100$$

Where OD_0 represents the absorbance of PFC/TPA@FNDs groups, OD_1 represents the absorbance of the NS group and OD_2 represents the absorbance of the deionized water group.

2.21. Cell viability assays

Cell viability assays were determined by CCK-8 assay as previously reported [33]. Human Oral Keratinocytes cells (HOK) were selected to verify the cytotoxicity of PFC/TPA@FNDs. Cells were seeded into a 96-well microtiter plate and co-cultured with different concentrations of the nanodroplets for 24 h in an incubator (5 % CO_2, 37 °C). The cell viability was measured by the CCK-8 assay and calculated using the following formula:

$$\text{Cell viability (\%)} = (OD_0\text{-}OD_1)/(OD_2\text{-}OD_1) *100$$

Where OD_0 represents the absorbance of PFC/TPA@FNDs groups, OD_1 represents the absorbance of the negative group (comprised of medium and CCK-8) and OD_2 represents the absorbance of the positive group (comprised of cells and CCK-8).

2.22. Tooth whitening experiments

To simulate natural teeth coloration, the teeth were soaked in a dye (a mixture of coffee, green tea, vinegar, and soy sauce) for 14 days and then rinsed with PBS until the eluent was colorless [34]. Experiments were divided into six groups: (1) PBS group: PBS (2.5 mL); (2) PFC/TPA@FNDs group: PFC/TPA@FNDs solution (0.2 mg/mL, 2.5 mL); (3) 7.5 % H_2O_2 group: 7.5 % H_2O_2 (2.5 mL); (4) 30 % H_2O_2 group: 30 % H_2O_2 (2.5 mL); (5) O_2@PFC/TPA@FNDs + Light group: PFC/TPA@FNDs solution (0.2 mg/mL, 2.5 mL) pretreated with O_2 bubbling and irradiated by a LED blue light (445 nm ± 5 nm, 56 mW/cm^2); (6) cold-light whitening: tooth whitening gel (25 % H_2O_2) + cold light irradiation (480 nm ~ 520 nm, 50 mW/cm^2, 30 min). After whitening for different durations (0 h, 3 h, 5 h), the teeth were photographed and contrasted with the change of color applied to dental professional color cards respectively. Subsequently, to observe the effect of tooth whitening on enamel, we observed the enamel of teeth from the above groups by SEM (Carl Zeiss AG Gemini 300).

2.23. Animal experiments

All animal procedures were performed in accordance with the Guidelines for Institutional Animal Care and Use Committee, and approved by the Animal Ethics Committee of Shanxi Medical University (No. SYDL2019002). Sprague-Dawley rats which were 21 days old were processed with adaptive feeding and antibiotic application. Then, the animals were infected with *S. mutans* for three consecutive days, and fed with the cariogenic diet and solution made of 5 % sucrose water and *S. mutans* suspension. Their infections were checked by oral swabbing plated onto BHI agar plates. The infected animals were randomly placed into seven groups (5 animals/group), and their teeth were treated using respective treatment every second day for three times then applied samples to the surface of teeth and irradiate with blue light for 10 min every time. The treatment groups included: (1) PBS group; (2) PBS + Light group; (3) PFC/TPA@FNDs group; (4) O_2@PFC/TPA@FNDs group; (5) PFC/TPA@FNDs + Light group; (6) O_2@PFC/TPA@MNDs + Light group; (7) O_2@PFC/TPA@FNDs + Light group. The group of healthy rats was regarded as control. The experiment proceeded for one week (7 days), and all animals were weighed at every stage. At the end of the experimental period, the rats were sacrificed, and the left maxillae were surgically removed and aseptically dissected. To evaluate the effect of biofilm disruption, the left maxillae was stained with 2 % basic fuchsin for 2 min, washed with water, and photographed to analyze the size of the staining area. For dental caries, the jaws of rats were imaged by Micro-CT and measured enamel thickness and caries depth. Finally, to observe smoothness of tooth surface, the enamels of the tooth were analyzed by SEM (Carl Zeiss AG Gemini 300).

2.24. Statistical analysis

All experimental data were repeated at least three times, and expressed as mean ± standard deviation (SD). The statistical difference was determined by *t*-test or one-way ANOVA. All the data are considered to have significant differences only when $p < 0.05$. *, ** and ***represent $p < 0.05$, $p < 0.01$, and $p < 0.001$, respectively.

3. Results and discussions

3.1. Fluorinated-polymer synthesis and nanodroplets preparation

The fluorinated-polymers were prepared by classical facile reversible addition-fragmentation chain transfer (RAFT) polymerization. Before polymerization, two hydrophobic monomers, fluorinated monomer (FMA) and 1-nonanol monomer (NMA) were synthesized first. The synthetic routes for monomer and polymer were shown in Fig. S1. 2H, 2H, 3H, 3H-Heptadecafluoroundecanoic acid was esterified with aminopropyl methacrylamide to afford FMA (Fig. S2). Previous studies have utilized fluorinated-polymer or fluorinated copolypeptide to fastly and robustly assemble with PFC to stabilize microbubbles behaving good ultrasound contrast ability [35,36]. NMA was also synthesized by reacting 1-nonanol with methacryloyl chloride to act as the hydrophobic segment for self-assembly with AIE photosensitizer (Fig. S3). PDMAEMA which can be protonated and be charged with high positive charge in acid condition was synthesized by RAFT polymerization (Fig. S4). Then, by copolymerize with FMA and NMA to afford fluorinated-polymers PDMAEMA-*b*-P(FMA-*co*-NMA) (Fig. S5). To compare with fluorinated-polymers, fluorinated-free-polymers PDMAEMA-*b*-PNMA were also synthesized by polymerizing PDMAEMA and NMA (Fig. S6). An AIE photosensitizer-TPA was acquired by a facile two-step synthesis [37] (Fig. S1 and Fig. S7). The maximum absorbance peak for TPA was in ~440 nm. To better calculate the TPA encapsulated efficacy in the later period, the calibration curve of TPA absorbance was tested in Figs. S8a–b. TPA has obvious AIE phenomenon which is highly emissive with the increase of poor solvent when excited by 445 nm light (Figs. S8c–e). PFC is one of the widely used ultrasound contrast agents in clinical and has high oxygen solubility [17]. Finally, PFC and TPA were formulated with PDMAEMA-*b*-P(FMA-*co*-NMA) by two-step emulsion process, affording PFC/TPA@FNDs. A control nanodroplet PFC/TPA@MNDs was also fabricated using similar method by replacing PDMAEMA-*b*-P(FMA-*co*-NMA) with PDMAEMA-*b*-PNMA.

PFC/TPA@FNDs were then characterized by different methods. The hydrodynamic diameters distribution of PFC/TPA@FNDs is about 190 nm measured by dynamic light scattering (DLS) (Fig. 1a). TEM results demonstrated PFC/TPA@FNDs have obvious and well-distributed hollow spherical morphology with the diameter ~100 nm, which revealed the successful encapsulation of PFC (Fig. 1b). The hollow spherical morphology was caused by gasification of PFC [26]. The TEM size is slightly less than DLS size, which may be due to the contribution from hydration layer resulted from hydrophilic PDMAEMA corona. In addition, the TEM sample is dried state under test and PFC have gasified resulting in the smaller PFC/TPA@FNDs cores. What's more, the absorbance spectra of TPA, FNPs (nanoparticles self-assembly by PDMAEMA-*b*-P(FMA-*co*-NMA)) and PFC/TPA@FNDs were analyzed (Fig. 1c). Compared with FNPs, PFC/TPA@FNDs have typical TPA peak in ~440 nm, which confirms the successful formation of nanodroplets. The TPA loading content is also calculated by using calibration curve of TPA absorbance and is determined by 10.21 % EE (Encapsulation Efficiency). Furthermore, the fluorescence emission spectra of TPA in DMSO and PFC/TPA@FNDs in H_2O were tested exciting by 445 nm laser (Fig. 1d). PFC/TPA@FNDs exhibited a strong fluorescence emission peaked at ~571 nm, while TPA has low fluorescence intensity, which confirm the TPA in PFC/TPA@FNDs is in aggregation state.

3.2. pH-responsive charge variation and loading efficiency

The pH-responsive charge variation of PFC/TPA@FNDs was analyzed by testing the zeta potentials of nanodroplets in different pH buffer (Fig. 1e). PFC/TPA@FNDs behaved extremely high positive charge for +14.87 mV in pH 4.4 compared with +3.99 mV in pH 8, which is similar to our previous results [26]. The acid environment responsive charge increasing phenomenon of PFC/TPA@FNDs is beneficial for nanodroplets deeply penetrating in biofilm.

The amount of PFC in nanodroplets was then detected by using gas chromatography (GC) (Fig. 1f). The PFC loading content was evaluated to be ~96.586 μL per 1 mg polymer and PFC loading efficiency was ~32.195 % for PFC/TPA@FNDs. Compared with PFC/TPA@MNDs, the PFC amount of PFC/TPA@FNDs is 1 time higher than PFC/TPA@MNDs,

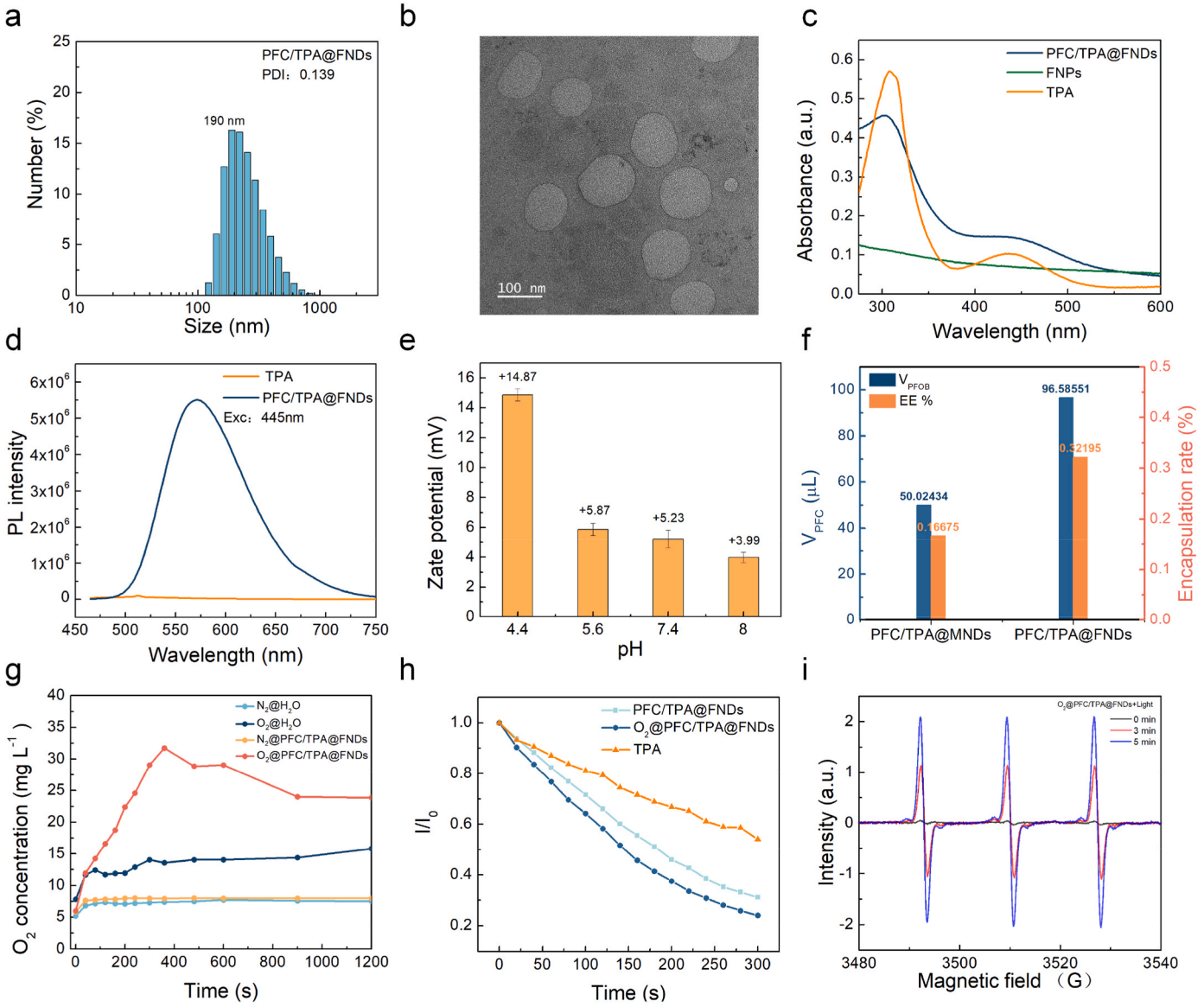

Fig. 1. Characterization of PFC/TPA@FNDs. (a) Hydrodynamic diameters distributions of PFC/TPA@FNDs; (b) TEM images of PFC/TPA@FNDs (Scale bar = 100 nm); (c) Absorbance spectra recorded for TPA, FNPs and PFC/TPA@FNDs; (d) Fluorescence emission spectra recorded for TPA in DMSO and PFC/TPA@FNDs in water, Exc: 445 nm; (e) Zeta potentials of PFC/TPA@FNDs in different pH solutions. (f) PFC loading amount (blue) and encapsulation efficiency (orange) of PFC/TPA@MNDs (fluorinated-free polymer) and PFC/TPA@FNDs; (g) Time dependent dissolved-oxygen concentrations of different samples. (h) ROS generation for O_2@PFC/TPA@FNDs, PFC/TPA@FNDs and TPA upon light irradiation (445 ± 5 nm, 56 mW/cm^2) using ABDA as indicator, normalized absorbance intensity at 400 nm. (i) $^1O_2$ generation of O_2@PFC/TPA@FNDs upon light irradiation (445 ± 5 nm, 56 mW/cm^2) for different time evaluated by EPR spectrometer, TEMP as indicator.

which revealed fluorinated-polymers have better PFC encapsulate effect and are good for oxygen load in the later stage. Then, the amounts of dissolved oxygen were detected by using the portable dissolved oxygen meter. PFC/TPA@FNDs had durable high dissolved oxygen amount with approximately 25 mg/L for long time, while O_2@H_2O group had a low dissolved oxygen amount with no more than 15.85 mg/L for the whole process (Fig. 1g). These results demonstrated PFC/TPA@FNDs constructed by fluorinated-polymers have great oxygen-carrying capacity and would be a good candidate as an oxygen-sufficient carrier.

3.3. ROS generation and bacterial adhesion

The ROS generation of PFC/TPA@FNDs was then investigated by using 9,10-Anthracenediyl-bis(methylene)dimalonic Acid (ABDA) as a detector (Figs. S9a–c) [38]. In O_2@PFC/TPA@FNDs group, the absorbance of ABDA decreased fast upon light (445 ± 5 nm) irradiation. On the condition without O_2 supply, the absorbance of ABDA decreased slower as for PFC/TPA@FNDs group. Moreover, in TPA group, the absorbance of ABDA decreased very slowly. The standardized ABDA absorbance results were as shown in Fig. 1h, O_2@PFC/TPA@FNDs behaved quickly ABDA absorbance decrease and had strong ROS generation ability. The results confirmed the oxygen is vital for PDT, and the photosensitive efficiency of AIE photosensitizer is enhanced when in aggregation state in nanodroplets. What's more, the $^1O_2$ generation of O_2@PFC/TPA@FNDs was further examined by using electron paramagnetic resonance (EPR) spectrometer, 2,2,6,6-Tetramethyl-4-piperidone (TEMP) as typical $^1O_2$ capture agent. With irradiation time prolong, the signal intensity rapidly enhance (Fig. 1i). These results confirmed the good ROS generation of nanodroplets.

Due to pH-responsive charge variation of PFC/TPA@FNDs, the PFC/TPA@FNDs were positively charged under acid environment. *S. mutans* is a major etiological agent of human dental caries and primarily resides

in oral biofilms [39]. In this paper, *S. mutans* is the main research object for treatment. *S. mutans* was co-cultured with PFC/TPA@FNDs in pH 4.5 for 0 min, 5 min, 15 min and 30 min, and then stained with SYTO 9, using CLSM to observe (Fig. 2a). The pink fluorescence of TPA and the green fluorescence of SYTO 9 represented nanodroplets and bacteria, respectively. The fluorescence of *S. mutans* was detected by using CLSM. *S. mutans* exhibited pink fluorescence in 5 min which revealed PFC/TPA@FNDs could fast adhere to bacteria. The pink fluorescence of *S. mutans* was pretty obvious in 30 min and had the best merge effect with green fluorescence of SYTO 9. In addition, to better quantify the merge ratio of two channel, Overlap Coefficient of each group was analyzed by Image J [40]. The 30 min incubation had the high Overlap Coefficient with r = 0.844. So, we chose 30 min as the point of time for nanodroplets co-cultured with *S. mutans*. What's more, we also used TEM to verify the bacterial adhesion of PFC/TPA@FNDs (Fig. 2b). Different from CLSM results, there were many nanodroplets around bacteria in 15 min. And nanodroplets could obviously adhere to bacteria in 30 min. In summary, PFC/TPA@FNDs have good bacterial adhesion ability which is benefit for bacteria killing.

3.4. Antibacterial activity and mechanism

To better therapy oral biofilm related diseases, the antibacterial ability of PFC/TPA@FNDs must be evaluated first. Minimum bactericidal concentration (MBC) is an important parameter for antibacterial ability evaluation, which is defined as the lowest concentration that kills 99.9 % (3logs) of the bacteria [41]. The *S. mutans* suspension (in pH 4.5) was pre-treated with O_2@PFC/TPA@FNDs for 30 min, and then conducted light irradiation or not. The O_2@PFC/TPA@FNDs + Light group behave good bacterial killing ability with MBC for 3.125 μg/mL, while for O_2@PFC/TPA@FNDs, the MBC is larger than 25 μg/mL (Fig. 2c–d). This result demonstrated the great photodynamic activity of O_2@PFC/TPA@FNDs. The representative photographs of corresponding bacterial colonies of *S. mutans* plate for different concentrations of O_2@PFC/TPA@FNDs were shown in Fig. 2d. As for O_2@PFC/TPA@FNDs + Light group, *S. mutans* plate almost had no bacteria colony when the concentration high than 3.125 μg/mL. Because of the good bacteria adhesion in pH 4.5, O_2@PFC/TPA@FNDs + Light group has good antibacterial ability. We also evaluated the antibacterial ability of O_2@PFC/TPA@FNDs in pH 7.4, the MBC was decreased to

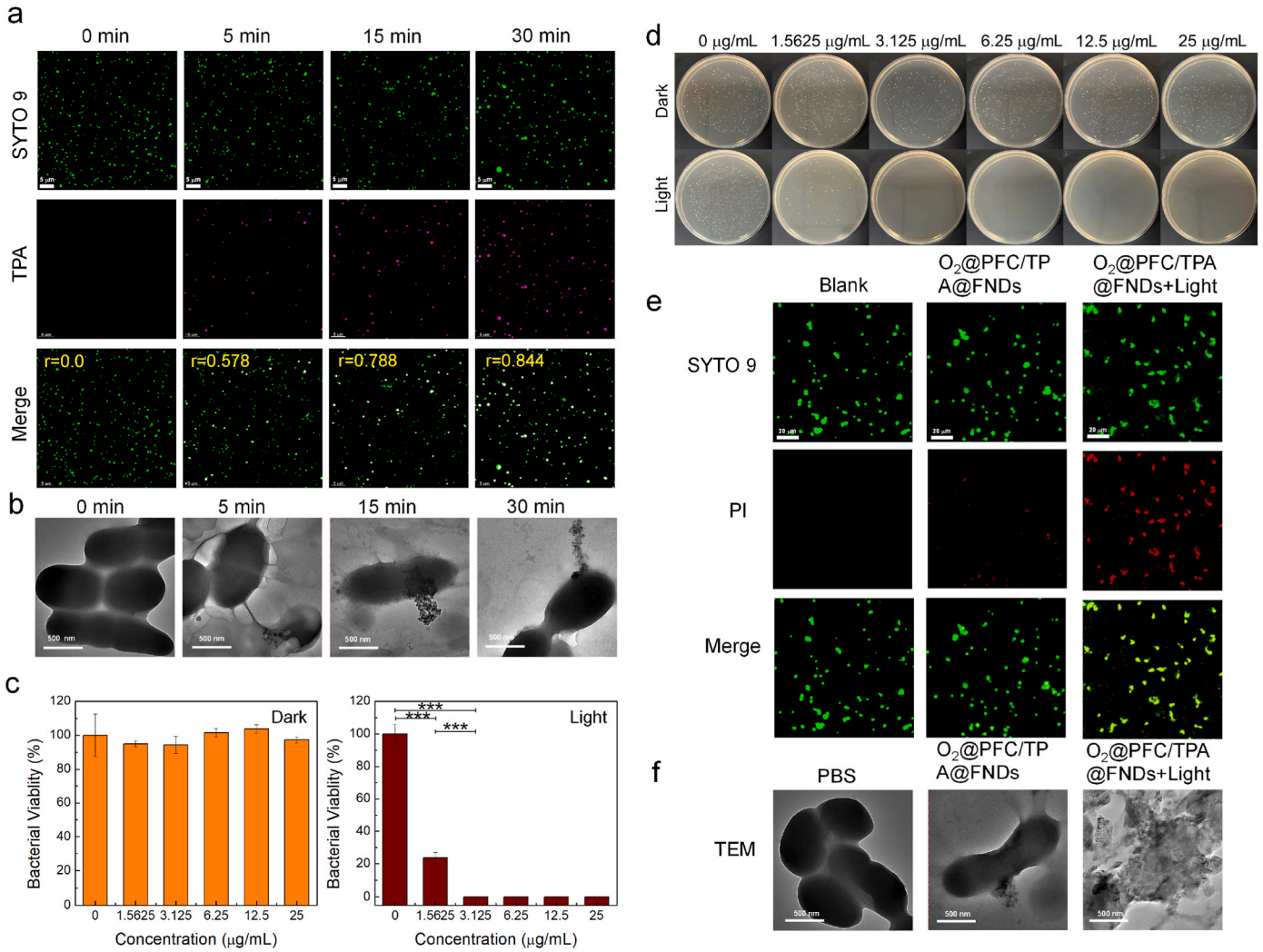

Fig. 2. Bacteria adhesion and bacteria killing assays. (a) CLSM images of PFC/TPA@FNDs incubated with *S. mutans* for different time, green and pink stains indicate bacteria and PFC/TPA@FNDs, Scale bar = 5 μm; (b) TEM images of PFC/TPA@FNDs incubated with *S. mutans* for different time, respectively, Scale bar = 500 nm; (c) Bacterial viability calculated by bacterial colony formation after treatment with different concentrations of O_2@PFC/TPA@FNDs upon light irradiation or not (*** represent $p < 0.001$); (d) Typical agar plates of different concentration of O_2@PFC/TPA@FNDs incubated with *S. mutans* upon light irradiation (445 ± 5 nm, 56 mW/cm^2) or not; (e) Fluorescence images of *S. mutans* upon treated with PBS or O_2@PFC/TPA@FNDs upon light irradiation (445 ± 5 nm, 56 mW/cm^2) or not respectively, and then stained with SYTO 9 and PI, green and red stains indicate live bacteria and dead bacteria, Scale bar = 20 μm; (f) TEM images of *S. mutans* upon treated with PBS or O_2@PFC/TPA@FNDs and upon light irradiation or not respectively, Scale bar = 500 nm.

6.25 μg/mL, which is slightly weaker than that in pH 4.5 (Fig. S10). To further evaluate antibacterial ability, Live/dead bacterial viability assay of *S. mutans* after incubated with O_2@PFC/TPA@FNDs and upon light irradiation or not were conducted. SYTO 9 can stain all the bacteria, while propidium iodide (PI) can stain dead bacteria which had damaged cell membrane [42]. For *S. mutans* + O_2@PFC/TPA@FNDs group the PI red fluorescence was weak, while there was intense red fluorescence of PI channel for *S. mutans* + O_2@PFC/TPA@FNDs + Light group, which also suggested the pretty good bacterial killing ability of the nanodroplets under light irradiation (Fig. 2e).

Due to the strong PI staining ability, the antibacterial mechanism of nanodroplets might be disruption of bacterial membrane. To verify the hypothesis, bacterial morphology after different treatment was observed by TEM. As shown in Fig. 2f, the normal *S. mutans* have smooth and intact membrane. After incubated with nanodroplets, there were a large amount of nanodroplets adhering to bacterial membrane. And upon light irradiation, obvious bacterial morphology changes occurred. Bacteria became very transparent and there seems no intracellular milieu inside bacteria which is caused by membrane disruption and further leading to leakage of intracellular milieu. Our result is similar to other's result that AIEgens can trigger ROS-mediated membrane damage and bacteria morphology collapsed and lysed [43]. To further evaluated the ROS level of bacteria after treatment, CLSM assays after treatment were conducted by using DCFH-DA. As show in Fig. S11, *S. mutans* has intensity green fluorescence after light irradiation, which confirmed the high ROS generation after PDT. Thus, O_2@PFC/TPA@FNDs is a good candidate for *S. mutans* killing and the antibacterial mechanism mainly depends on ROS-mediated membrane damage.

3.5. Antibiofilm activity

Most bacterial infections are associated with biofilm, *S. mutans* could use adequate nutrition in oral environment and adhere tooth to form biofilm. There are anaerobic zones in deep biofilm, which cause low therapeutical effect for oxygen-related dynamic therapy. And then, we evaluate the antibiofilm ability of nanodroplets. After incubated *S. mutans* in well plates for 48 h, the *S. mutans* biofilm could obviously observed in the bottom. Different groups (PBS, PFC/TPA@MNDs, PFC/TPA@FNDs, O_2@PFC/TPA@MNDs, O_2@PFC/TPA@FNDs) upon light irradiation or not have been treated in *S. mutans* biofilm. The residue biofilm was counted using the plate count method. Both O_2@PFC/TPA@MNDs and O_2@PFC/TPA@FNDs behave good antibiofilm ability upon light irradiation, while PFC/TPA@FNDs is better than PFC/TPA@MNDs, which may be caused by the high oxygen loading efficacy of PFC/TPA@FNDs (Fig. 3a–b). Compared with control group, O_2@PFC/TPA@FNDs + Light could eliminate more than 99 % biofilm. The nanodroplets behaved highly efficient antibiofilm ability owing to acid environment-responsive positive charge enhancement and oxygen relive biofilm hypoxia environment strategies.

Furthermore, after incubated *S. mutans* biofilm in the PMMA slice, the bacterial Live/dead viability assay also was conducted to evaluate the antibiofilm ability by using CLSM (Fig. 3c). *S. mutans* was stained by SYTO 9 (green channel) and PI (red channel) for distinguish live and dead. The first and second columns refer to 2D bottom and middle CLSM images, and the third and fourth columns refer to 3D merge and 3D PI CLSM images. There was thick and compact green fluorescence in control and control + Light group, confirming the successful biofilm culture and light have no obvious effect on biofilm. While, for O_2@PFC/TPA@FNDs + Light, there was strong yellow fluorescence in biofilm (green and red fluorescence merge) and the thinnest residue biofilm area, which indicated the good bacterial killing ability and antibiofilm ability. These results demonstrated O_2@PFC/TPA@FNDs could efficiently ablate *S. mutans* biofilm by enhanced PDT effects.

What's more, we cultured *S. mutans* biofilm in hydroxyapatite discs to simulate the main components of teeth. After *S. mutans* biofilm grown in hydroxyapatite discs, different treatments (PBS, O_2@PFC/TPA@FNDs and O_2@PFC/TPA@FNDs + Light) have been applied. Then, the SEM images of bacteria biofilm were recorded (Fig. S12a). Compared with control group and O_2@PFC/TPA@FNDs group, the bacteria amount obviously decreased, and there were many poles in the bacteria surface. These results confirmed ROS-mediated membrane damage. *S. mutans* is the leading cause for dental caries, and then we cultured *S. mutans* with tooth *in vitro* to form *S. mutans* biofilm. We also evaluated the antibiofilm ability of PFC/TPA@FNDs for *S. mutans* biofilm in tooth by using SEM. As shown in Fig. 3d, compared with control group, O_2@PFC/TPA@FNDs + Light has less bacteria amount. What's more, the bacteria morphology has obvious wrinkle. However, the thick and dense layer of bacteria in control group is smooth and intact. Although O_2@PFC/TPA@FNDs group also has less bacteria amount, the residue bacteria had good viability because of the normal morphology. The AIE-photosensitizer puts into great play PDT ability when encapsulated in nanodroplet and with oxygen self-sufficient ability. Proteins is a typical component in EPS. We further evaluated the protein production in EPS after PDT treatment using BCA Protein Assay Kit. As shown in Fig. S12b, O_2@PFC/TPA@FNDs + Light group has lowest protein production in EPS, could reduce approximately 60 % protein production compared with PBS group. The result confirmed O_2@PFC/TPA@FNDs-related PDT could reduce protein production in biofilm. To sum up, O_2@PFC/TPA@FNDs has good antibiofilm ability, which may be a good candidate for oral biofilm eradication.

Due to the good antibiofilm ability of PFC/TPA@FNDs, we used 3D confocal imaging to validate the bacterial penetration ability of PFC/TPA@FNDs. Bacteria were stained by SYTO 9, which behave green fluorescence. TPA in PFC/TPA@FNDs are in aggregation-state which has strong pink fluorescence after excited by 450 nm laser. After incubation of PFC/TPA@FNDs with *S. mutans* biofilm, pink fluorescence began in 15 min (Fig. 3e). And with the incubation time extended to 30 min, pink fluorescence became strong and widely distributed. These results confirmed PFC/TPA@FNDs can deeply penetrate bacteria biofilm, which might due to the acid-responsive positive-charge enhancement. The positive charge of nanodroplet is good for particles penetrating and retaining in biofilm, because EPS and bacteria usually are negatively charged. So, PFC/TPA@FNDs could realize the prerequisite of antibiofilm, it can quickly penetrate and retain in biofilm, then give full play to PDT effect killing bacteria and antibiofilm.

3.6. Biocompatibility and hemolysis

Prior to applying nanodroplets to animal model, cell viability and hemolysis assays were conducted first. Human Oral Keratinocytes cells (HOK) were selected for CCK-8 assay. Cells were cultured with PFC/TPA@FNDs for 24 h, and then evaluated cell viability by using CCK-8 kit. As shown in Fig. 4a, even in the concentration of 200 μg/mL nanodroplets behaved no obvious effect for HOK cells (~85 % cell viability), which implied good cell biosafety. Hemolysis assays were also performed by using rat's red blood cells (RBCs) [44]. There was no obvious hemolysis reaction observed for nanodroplets concentration from 3.125 μg/mL to 200 μg/mL, and hemolysis ratio were determined below 5 % (Fig. 4b). So, nanodroplets even applied in oral environment and entered bloodstream inevitably, would not have obvious hemolysis reaction.

3.7. Animal experiment

Biofilm is the main cause of dental caries. Biofilm eradication is important for dental caries therapy. Because of the good PDT ability and excellent antibiofilm ability, we evaluated the potential of caries inhibition of nanodroplets in animal model. As shown in Fig. 5a, Sprague-Dawley rats processed with adaptive feeding, antibiotic treatment, *S. mutans* infection and cariogenic diet established dental caries animal model. After *S. mutans* colonized in teeth and developed to *S. mutans* biofilm, different microstructures of teeth (including enamel and dentin)

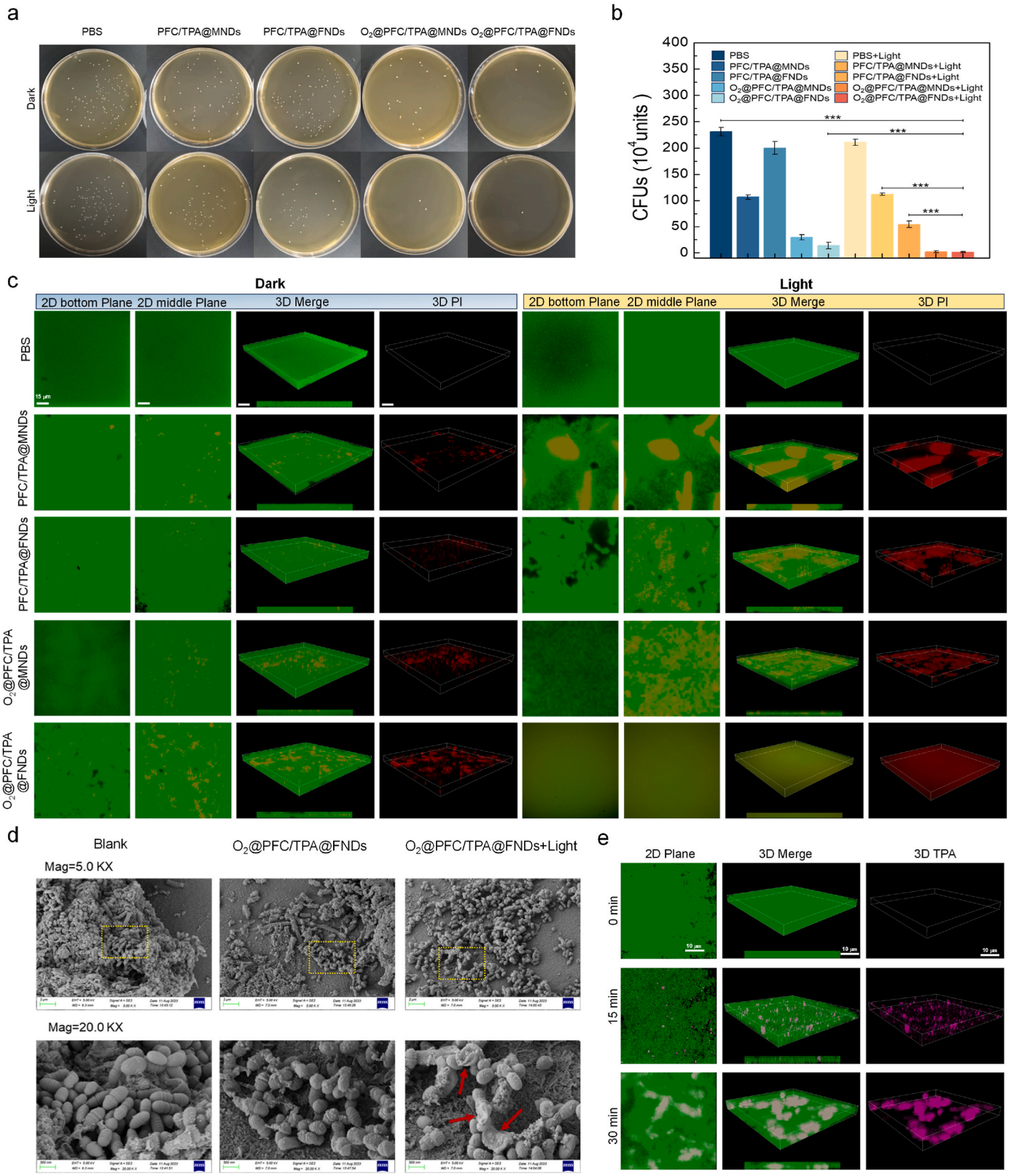

Fig. 3. Antibiofilm and biofilm penetration. (a) Typical agar plates of different samples incubate with *S. mutans* biofilm and then irradiate light or not using a plate counting method; (b) Bacterial colony counts of *S. mutans* biofilm after treatment with different samples upon irradiation light (445 ± 5 nm, 56 mW/cm^2) or not (*** represent $p < 0.001$). (c) 2D and 3D CLSM images of different samples incubated with *S. mutans* biofilm upon irradiation light (445 ± 5 nm, 56 mW/cm^2) or not, and then stained by SYTO 9 (green channel) and PI (red channel). The first and second columns refer to 2D bottom and middle CLSM images, and the third and fourth columns refer to 3D merge and 3D PI CLSM images, Scale bar = 15 μm; (d) Different magnification SEM images of *S. mutans* biofilm (in teeth) incubated with PBS, O_2@PFC/TPA@FNDs upon light irradiation or not, the red arrows refer to the disrupted bacterial morphology, Scale bar = 2 μm and 500 nm for top and down lines; (e) 2D and 3D CLSM images of PFC/TPA@FNDs incubate with *S. mutans* biofilm for different time, green and pink stains indicate bacteria and nanodroplets, Scale bar = 10 μm.

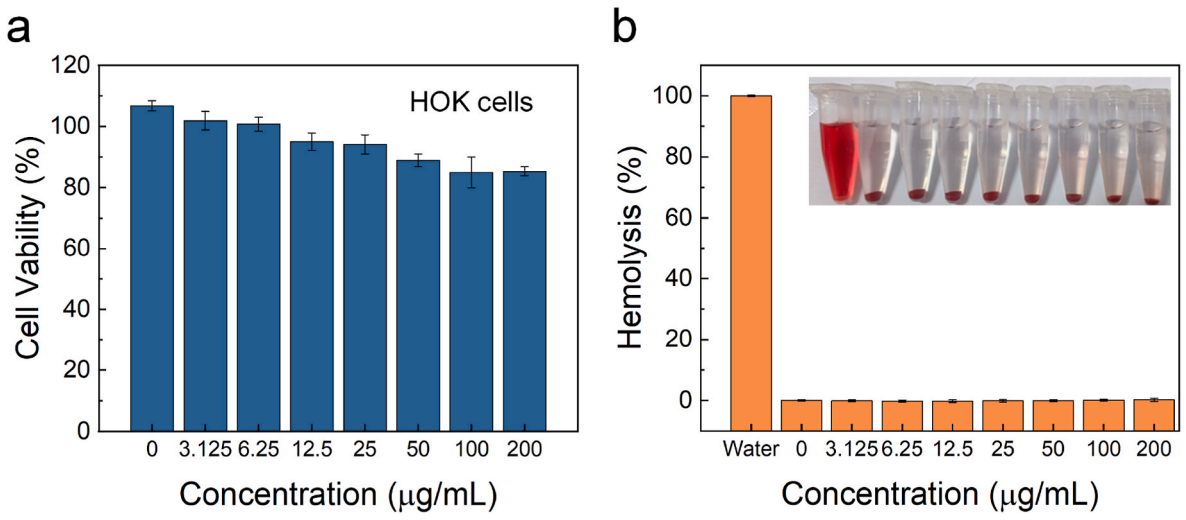

Fig. 4. Biosafety of nanodroplets. (a) Evaluation the cytotoxicity of different concentrations PFC/TPA@FNDs to Human Oral Keratinocytes cells (HOK); (b) Hemolysis ratio of different concentrations of PFC/TPA@FNDs, Inset: representative images for the hemolytic analysis.

can be damaged. PBS, PFC/TPA@FNDs, O_2@PFC/TPA@FNDs, and O_2@PFC/TPA@MNDs were topically applied on occlusal surface and then conducted light irradiation or not every other day for 3 times.

The good antibiofilm ability of O_2@PFC/TPA@FNDs have been confirmed in previous assays. So, we evaluated the dental plaque formed by bacterial biofilms using basic fuchsin stain after treatment, firstly. As shown in Fig. 5b, the teeth of O_2@PFC/TPA@FNDs + Light group have less stained area compared with other groups (yellow arrows sites). As for the untreated group (PBS), large area of biofilms existed on the tooth surface. These results suggest after encapsulating O_2, PFC/TPA@FNDs could behave good antibiofilm ability upon light irradiation resulting in little basic fuchsin stained area with little biofilm distribution.

Secondly, the microstructure of teeth after treatment has been revealed by SEM detection. As shown in Fig. 5c, the healthy tooth had a smooth surface, and smoothness was pretty good even in the cracks in an enlarged field of view. While for untreated group (PBS), the microstructure of tooth was very rough in an enlarged field of view, which revealed the disruption of tooth caused by bacterial biofilm. In O_2@PFC/TPA@FNDs + Light group, the smoothness of the tooth was similar to healthy tooth, which had pretty good smoothness. The results indicated the high efficiency and thorough antibiofilm ability of nanodroplets can protect teeth from dental caries.

Thirdly, Mirco-CT images of teeth after therapy have been acquired to analyze the dental caries sites. The cross-sectional view of teeth could be clearly shown by using 3D Micro-CT. Two main parameters, enamel thickness and caries depth were finely measured adopting the same standard by using CTAn software at pit and fissure gap sites. As shown in Fig. 5d, the healthy tooth has large enamel thickness (red line) and little caries depth (yellow line) with parameters for 0.2 mm and 0.35 mm. After dental caries occurred, the enamel would be disrupted and even dentin would be affected. Compared with healthy tooth, the tooth of untreated group (PBS) has little enamel thickness and large caries depth with parameters for 0.131 mm and 0.623 mm, suggesting the successful establishment of the dental caries animal model. After O_2@PFC/TPA@FNDs + Light treatment, the tooth is similar to a healthy tooth which has large enamel thickness and little caries depth with parameters for 0.182 mm and 0.466 mm, suggesting the good caries prevention ability of nanodroplets. What's more, the two parameters of teeth in all the groups have a sum in Fig. 5e. O_2@PFC/TPA@FNDs + Light group has obvious therapeutic effects, which could high efficiently eliminate biofilm and prevent dental caries.

Under treatment process, the rat weights of different groups have been recorded (Fig. S13). The rat weights gradually increased with time, revealing all the treatments have no obvious effect for rat health. In addition, after therapeutic process, H&E staining analysis of major organs (heart, liver, spleen, lung, and kidney) was conducted to evaluate the potential toxicity of nanodroplets (Fig. S14). There was no abnormality in different groups, suggesting the acceptable biocompatibility of nanodroplets when used for dental caries prevention. In conclusion, PFC/TPA@FNDs could behave good antibiofilm ability to prevent dental caries and have good biocompatibility, which maybe a potential candidate for oral biofilm elimination.

3.8. Tooth whitening

The good ROS generation of nanodroplets may endow it tooth whitening ability. Habitual intake of colored foods (coffee, tea, and juice) and imperfect teeth cleaning are leading causes for teeth discoloration [13]. H_2O_2 and carbamide peroxide are two clinical tooth-whitening agents, which could oxidize stains and pigment to behave tooth-whitening function. Although H_2O_2 has excellent tooth whitening ability, it can destroy microstructure of tooth enamel and result dentine hypersensitivity [30]. Because of the good ROS generation ability of AIE photosensitizer, we infer PFC/TPA@FNDs have good tooth-whitening effect. After soaked human teeth in a mixed liquid (coffee, green tea, vinegar, and soy sauce) for 15 days, different samples were added and then conducted light irradiation or not (Fig. 6a). According to the dental professional color card [45] (Fig. 6b), the tooth treated with O_2@PFC/TPA@FNDs and upon light irradiation was discernably whitened from C_2 to B_1 after 5 h of whitening, a six-level whitening change, which is better than PBS (from C_4 to C_4) and similar to the effect of 7.5 % H_2O_2 (from C_4 to D_3). As a widely used bleaching technique, cold-light bleaching technique behave effective bleaching ability in discolored teeth by using blue light (480 nm ~ 520 nm). After using tooth whitening gel (25 % Hydrogen peroxide) and irradiation cold light (50 mW/cm^2) for 30 min, the tooth whitening effect is slightly superior than O_2@PFC/TPA@FNDs + light (C_4 to D_3 VS C_2 to B_1). While, cold light whitening need use desensitizer to decrease tooth sensitivity [46], and some research pointed the potential enamel surface demineralization and after cold-light bleaching mainly caused by the acidic peroxide-containing bleaching agent [47].

After the process of tooth-whitening, teeth structures of different groups were examined by SEM (Fig. 6c). The morphology after photodynamic whitening with PFC/TPA@FNDs is similar to healthy tooth, which has smooth and regular surface. The cold light whitening group had rough surface but no pittings and holes. While for 30 % H_2O_2 group,

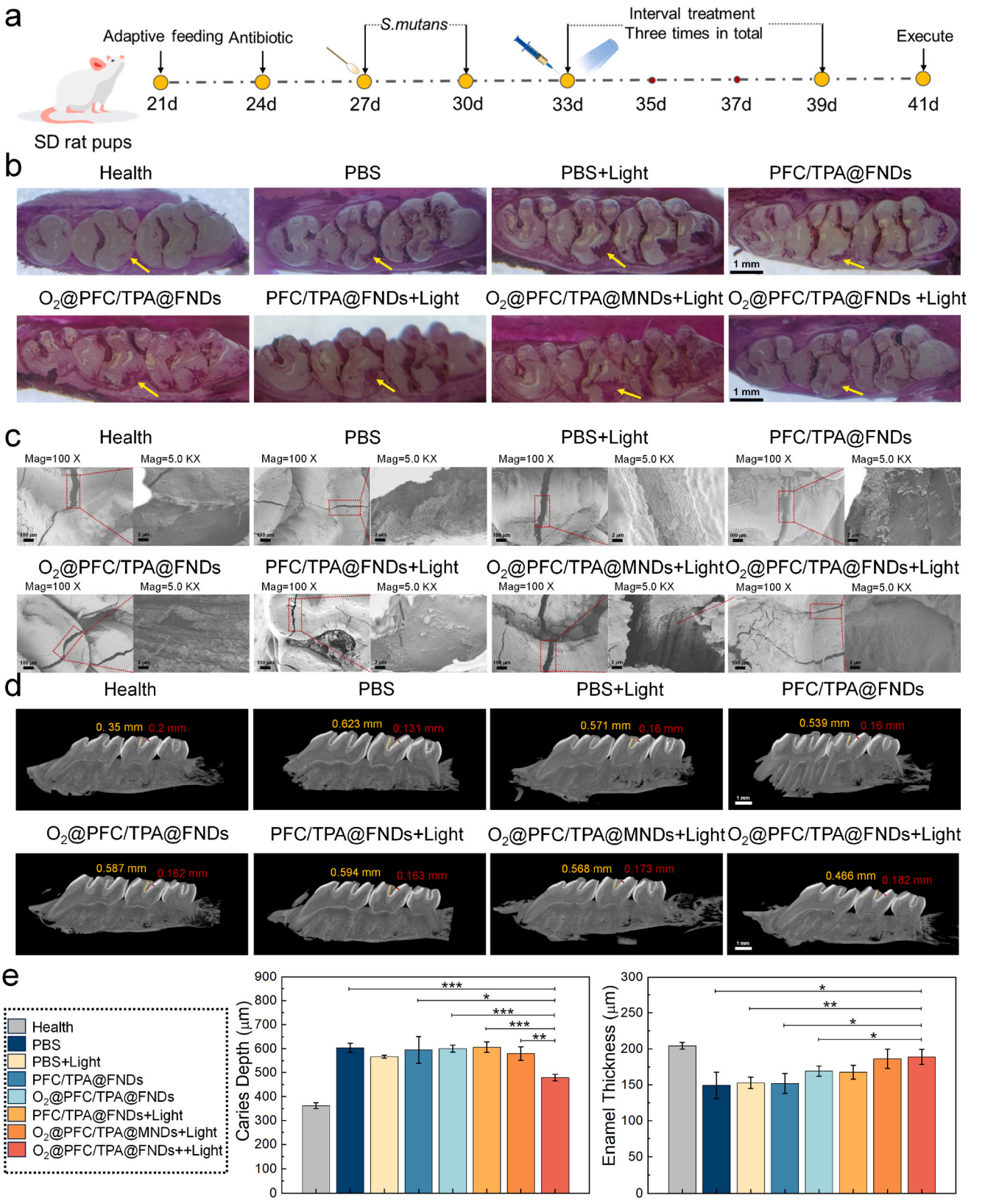

Fig. 5. Animal dental caries model evaluating the therapeutic effect of nanodroplets. (a) Schematic illustration of the construction of dental caries animal model and the therapeutic process. (b) Images of basic fuchsin stained plaque after different treatments, yellow arrows showed the biofilm areas on the surface of tooth, Scale bar = 1 mm. (c) Different magnification SEM images of teeth in different groups after treatment, the microstructures of teeth surface were different, Scale bar = 100 μm and 2 μm respectively. (d) The cross-sectional view of Micro-CT results for teeth in different groups. Enamel thickness and caries depth were labeled by red line and yellow line respectively, and the numbers were calculated by CTAn software, Scale bar = 1 mm. (e) The summary of enamel thickness and caries depth in different groups, recorded by CTAn software (*, **, *** represent $p < 0.05$, $p < 0.01$ and $p < 0.001$).

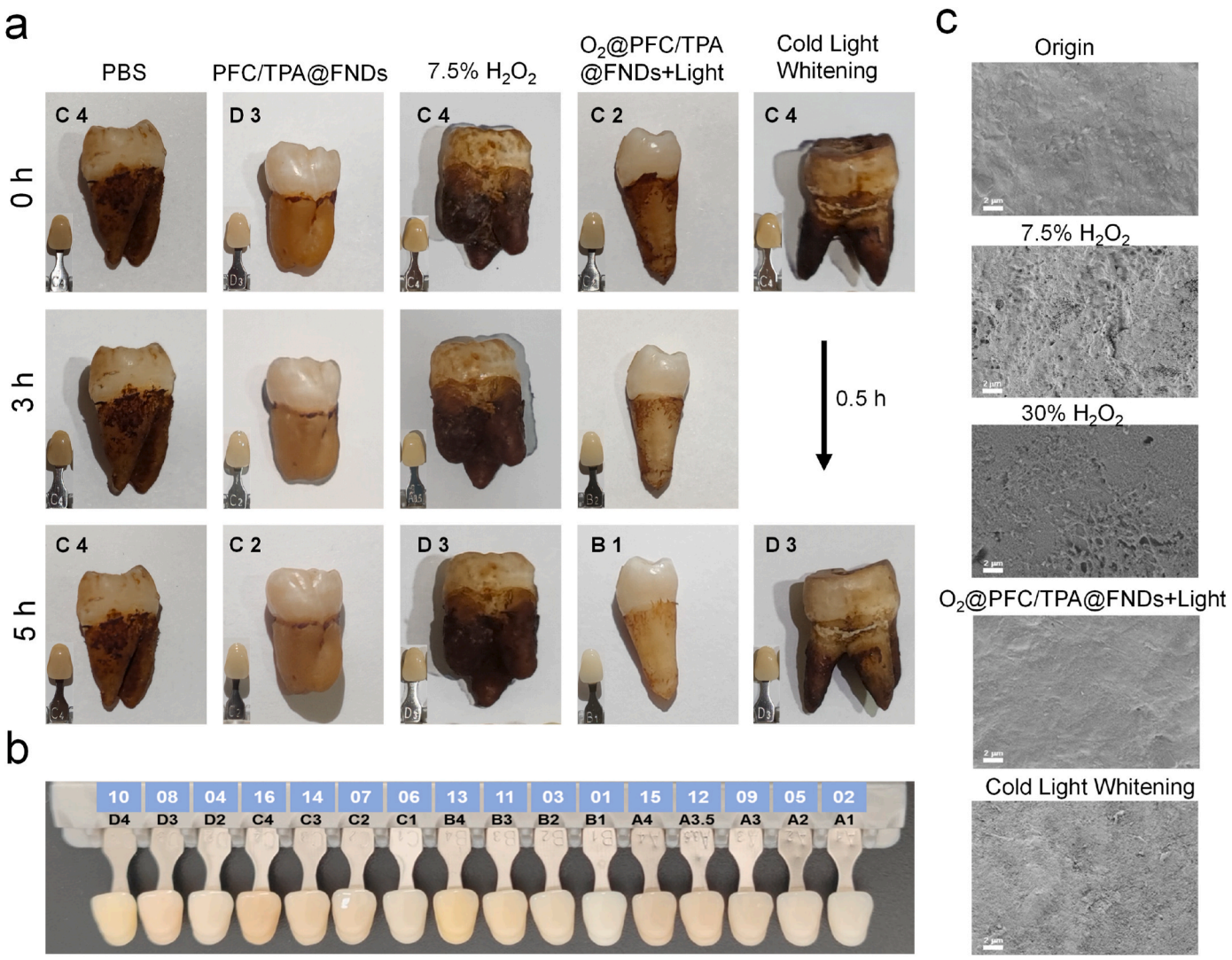

Fig. 6. Tooth whitening effect of nanodroplets and biocompatibility. (a) Photographs of teeth-stained color and then treated with PBS, PFC/TPA@FNDs, 7.5 % H_2O_2, O_2@PFC/TPA@FNDs + Light for 0, 3, 5 h and cold-light whitening (30 min), respectively; (b)VITA classical shade guide for tooth color; (c)SEM images of healthy teeth and teeth treated with 7.5 % H_2O_2, 30 % H_2O_2, O_2@PFC/TPA@FNDs + Light, and cold-light whitening, Scale bar = 2 μm.

the teeth were damaged and eroded, exhibiting pittings and holes, which is similar to other's conclusion [34]. What's more, 7.5 % H_2O_2 had few pittings and holes compared with 30 % H_2O_2 which have comparable safety for short-time use. Compared with clinical technologies, although PFC/TPA@FNDs had a slightly inferior whitening effect, the controllable, local, high ROS generation result harmless nature to tooth which maybe a good candidate for tooth-whitening agent.

4. Conclusion

In summary, we fabricated an oxygen self-sufficient nanodroplet based on fluorinated polymer and an AIE-photosensitizer. The nanodroplet could be protonized with enhancement positive charge under acid biofilm environment, deeply penetrate biofilm and quickly adhere to bacteria. The extremely high PFC and oxygen loading efficacy of nanodroplets could relieve the hypoxia environment of biofilm. The aggregated AIE-photosensitizer in nanodroplets could behave high-efficient PDT ability to eliminate bacterial biofilm. Animal dental caries assays suggested the potential of nanodroplets for dental caries prevention. *Ex vivo* tooth whitening assay also proved the superiority to H_2O_2, without damage to tooth surface. Overall, the fluorinated-polymer fabricated oxygen self-sufficient nanodroplet is a promising antibacterial platform for treatment of dental caries and other oral biofilm-related diseases.

CRediT authorship contribution statement

Bing Cao: Writing – review & editing, Writing – original draft, Resources, Methodology, Conceptualization. **Yingfei Ma:** Writing – review & editing, Investigation, Conceptualization. **Jian Zhang:** Writing – review & editing, Investigation. **Yanan Wang:** Methodology. **Yating Wen:** Methodology. **Yun li:** Methodology. **Ruixue Wang:** Methodology. **Donghai Cao:** Methodology. **Ruiping Zhang:** Supervision, Resources, Methodology, Conceptualization.

Declaration of competing interest

The authors declare that they have no known competing financial interests or personal relationships that could have appeared to influence the work reported in this paper.

Data availability

Data will be made available on request.

Acknowledgements

This work has been financially by National Key R&D Program of China (NO: 2023YFC3402800), National Natural Science Foundation of China (No: 82120108016, 82071987), Key Laboratory of Nano-imaging and Drug-loaded Preparation of Shanxi Province (NO: 202104010910010), Shanxi Province Science Foundation for Youths (NO: 20210302124035, 20210302124285, 202203021212090), Scientific Research Foundation of Shanxi Bethune Hospital (NO: 2022RC14), National Natural Science Foundation Seed Player Project of Shanxi Bethune Hospital (NO: 2023GZRZ02). The authors also acknowledge the Medical Experimental Center of Shanxi Bethune Hospital for providing the necessary equipment for this work.

Appendix A. Supplementary data

Supplementary data to this article can be found online at https://doi.org/10.1016/j.mtbio.2024.101091.

References

[1] U. Romling, S. Kjelleberg, S. Normark, L. Nyman, B.E. Uhlin, B. Akerlund, Microbial biofilm formation: a need to act, J. Intern. Med. 276 (2) (2014) 98–110, https://doi.org/10.1111/joim.12242.

[2] W.H. Bowen, R.A. Burne, H. Wu, H. Koo, Oral biofilms: pathogens, matrix, and polymicrobial interactions in microenvironments, Trends Microbiol. 26 (3) (2018) 229–242, https://doi.org/10.1016/j.tim.2017.09.008.

[3] H.C. Flemming, J. Wingender, The biofilm matrix, Nat. Rev. Microbiol. 8 (9) (2010) 623–633, https://doi.org/10.1038/nrmicro2415.

[4] H.C. Flemming, J. Wingender, U. Szewzyk, P. Steinberg, S.A. Rice, S. Kjelleberg, Biofilms: an emergent form of bacterial life, Nat. Rev. Microbiol. 14 (9) (2016) 563–575, https://doi.org/10.1038/nrmicro.2016.94.

[5] M.A. Peres, L.M.D. Macpherson, R.J. Weyant, B. Daly, R. Venturelli, M.R. Mathur, S. Listl, R.K. Celeste, C.C. Guarnizo-Herreno, C. Kearns, H. Benzian, P. Allison, R. G. Watt, Oral diseases: a global public health challenge, Lancet 394 (10194) (2019) 249–260, https://doi.org/10.1016/S0140-6736(19)31146-8.

[6] A.J. Righolt, M. Jevdjevic, W. Marcenes, S. Listl, Global-, regional-, and country-level economic impacts of dental diseases in 2015, J. Dent. Res. 97 (5) (2018) 501–507, https://doi.org/10.1177/0022034517750572.

[7] D.S.W. Benoit, K.R. Sims Jr., D. Fraser, Nanoparticles for oral biofilm treatments, ACS Nano 13 (5) (2019) 4869–4875, https://doi.org/10.1021/acsnano.9b02816.

[8] M. Kolarikova, B. Hosikova, H. Dilenko, K. Barton-Tomankova, L. Valkova, R. Bajgar, L. Malina, H. Kolarova, Photodynamic therapy: innovative approaches for antibacterial and anticancer treatments, Med. Res. Rev. 43 (4) (2023) 717–774, https://doi.org/10.1002/med.21935.

[9] F. Xiao, B. Cao, L. Wen, Y. Su, M. Zhan, L. Lu, X. Hu, Photosensitizer conjugate-functionalized poly(hexamethylene guanidine) for potentiated broad-spectrum bacterial inhibition and enhanced biocompatibility, Chin. Chem. Lett. 31 (9) (2020) 2516–2519, https://doi.org/10.1016/j.cclet.2020.06.038.

[10] Y. Liu, K. Yang, J. Wang, Y. Tian, B. Song, R. Zhang, Hypoxia-triggered degradable porphyrinic covalent organic framework for synergetic photodynamic and photothermal therapy of cancer, Mater. Today Bio 25 (2024) 100981, https://doi.org/10.1016/j.mtbio.2024.100981.

[11] S.S. Lucky, K.C. Soo, Y. Zhang, Nanoparticles in photodynamic therapy, Chem. Rev. (Washington, DC, U. S.) 115 (4) (2015) 1990–2042, https://doi.org/10.1021/cr5004198.

[12] Y.X. Ge, H.J. Zhuang, T.W. Zhang, H.F. Liang, W. Ding, L. Zhou, Z.R. Dong, Z. C. Hu, Q. Chen, J. Dong, L.B. Jiang, X.F. Yin, Precise manipulation of circadian clock using MnO(2) nanocapsules to amplify photodynamic therapy for osteosarcoma, Mater. Today Bio 19 (2023) 100547, https://doi.org/10.1016/j.mtbio.2023.100547.

[13] H. Zhang, Y. Zhu, Y. Li, X. Qi, J. Yang, H. Qi, Q. Li, Y. Ma, Y. Zhang, X. Zhang, L. Zhang, A bifunctional Zwitterion-modified porphyrin for photodynamic nondestructive tooth whitening and biofilm eradication, Adv. Funct. Mater. 31 (42) (2021) 2104799, https://doi.org/10.1002/adfm.202104799.

[14] N.C. Araujo, C.R. Fontana, V.S. Bagnato, M.E. Gerbi, Photodynamic antimicrobial therapy of curcumin in biofilms and carious dentine, Laser Med. Sci. 29 (2) (2014) 629–635, https://doi.org/10.1007/s10103-013-1369-3.

[15] M. Hirose, Y. Yoshida, K. Horii, Y. Hasegawa, Y. Shibuya, Efficacy of antimicrobial photodynamic therapy with Rose Bengal and blue light against cariogenic bacteria, Arch. Oral Biol. 122 (2021) 105024, https://doi.org/10.1016/j.archoralbio.2020.105024.

[16] J. Jagers, A. Wrobeln, K.B. Ferenz, Perfluorocarbon-based oxygen carriers: from physics to physiology, Pflügers Archiv 473 (2) (2021) 139–150, https://doi.org/10.1007/s00424-020-02482-2.

[17] Y. Cheng, H. Cheng, C. Jiang, X. Qiu, K. Wang, W. Huan, A. Yuan, J. Wu, Y. Hu, Perfluorocarbon nanoparticles enhance reactive oxygen levels and tumour growth inhibition in photodynamic therapy, Nat. Commun. 6 (2015) 8785, https://doi.org/10.1038/ncomms9785.

[18] X. Sun, J. Sun, Y. Sun, C. Li, J. Fang, T. Zhang, Y. Wan, L. Xu, Y. Zhou, L. Wang, B. Dong, Oxygen self-sufficient nanoplatform for enhanced and selective antibacterial photodynamic therapy against anaerobe-induced periodontal disease, Adv. Funct. Mater. 31 (20) (2021) 2101040, https://doi.org/10.1002/adfm.202101040.

[19] W. Wang, Y. Hu, Z. Chen, L. Yu, S. Huang, Y. Zhang, J. Li, Y. Xue, A. Li, Y. Wang, Z. Wu, X. Zhang, Guanidine and galactose decorated nanophotosensitizer with oxygen self-sufficient capability for the localized ablation of oral biofilm, Adv. Funct. Mater. 33 (37) (2023) 2300474, https://doi.org/10.1002/adfm.202300474.

[20] F. Hu, S. Xu, B. Liu, Photosensitizers with aggregation-induced emission: materials and biomedical applications, Adv. Mater. 30 (45) (2018) 1801350, https://doi.org/10.1002/adma.201801350.

[21] S. Liu, G. Feng, B.Z. Tang, B. Liu, Recent advances of AIE light-up probes for photodynamic therapy, Chem. Sci. 12 (19) (2021) 6488–6506, https://doi.org/10.1039/d1sc00045d.

[22] B. Li, W. Wang, L. Zhao, D. Yan, X. Li, Q. Gao, J. Zheng, S. Zhou, S. Lai, Y. Feng, J. Zhang, H. Jiang, C. Long, W. Gan, X. Chen, D. Wang, B.Z. Tang, Y. Liao, Multifunctional AIE nanosphere-based "nanobomb" for trimodal imaging-guided photothermal/photodynamic/pharmacological therapy of drug-resistant bacterial infections, ACS Nano 17 (5) (2023) 4601–4618, https://doi.org/10.1021/acsnano.2c10694.

[23] J. Zheng, T. Chen, K. Wang, C. Peng, M. Zhao, Q. Xie, B. Li, H. Lin, Z. Zhao, Z. Ji, B. Z. Tang, Y. Liao, Engineered multifunctional zinc-organic framework-based aggregation-induced emission nanozyme for accelerating spinal cord injury recovery, ACS Nano 18 (3) (2024) 2355–2369, https://doi.org/10.1021/acsnano.3c10541.

[24] Z. Zhang, M. Kang, H. Tan, N. Song, M. Li, P. Xiao, D. Yan, L. Zhang, D. Wang, B. Z. Tang, The fast-growing field of photo-driven theranostics based on aggregation-induced emission, Chem. Soc. Rev. 51 (6) (2022) 1983–2030, https://doi.org/10.1039/d1cs01138c.

[25] J.M.V. Makabenta, A. Nabawy, C.H. Li, S. Schmidt-Malan, R. Patel, V.M. Rotello, Nanomaterial-based therapeutics for antibiotic-resistant bacterial infections, Nat. Rev. Microbiol. 19 (1) (2021) 23–36, https://doi.org/10.1038/s41579-020-0420-1.

[26] B. Cao, X. Lyu, C. Wang, S. Lu, D. Xing, X. Hu, Rational collaborative ablation of bacterial biofilms ignited by physical cavitation and concurrent deep antibiotic release, Biomaterials 262 (2020) 120341, https://doi.org/10.1016/j.biomaterials.2020.120341.

[27] B. Horev, M.I. Klein, G. Hwang, Y. Li, D. Kim, H. Koo, D.S. Benoit, pH-activated nanoparticles for controlled topical delivery of farnesol to disrupt oral biofilm virulence, ACS Nano 9 (3) (2015) 2390–2404, https://doi.org/10.1021/nn507170s.

[28] C. Wang, W. Zhao, B. Cao, Z. Wang, Q. Zhou, S. Lu, L. Lu, M. Zhan, X. Hu, Biofilm-responsive polymeric nanoparticles with self-adaptive deep penetration for in vivo photothermal treatment of implant infection, Chem. Mater. 32 (18) (2020) 7725–7738, https://doi.org/10.1021/acs.chemmater.0c02055.

[29] M. Gao, C. Liang, X. Song, Q. Chen, Q. Jin, C. Wang, Z. Liu, Erythrocyte-membrane-enveloped perfluorocarbon as nanoscale artificial red blood cells to relieve tumor hypoxia and enhance cancer radiotherapy, Adv. Mater. 29 (35) (2017) 1701429, https://doi.org/10.1002/adma.201701429.

[30] M. Gu, S. Jiang, X. Xu, M.Y. Wu, C. Chen, Y. Yuan, Q. Chen, Y. Sun, L. Chen, C. Shen, P. Guo, S. Liu, E. Zhao, S. Chen, S. Chen, Simultaneous photodynamic eradication of tooth biofilm and tooth whitening with an aggregation-induced emission luminogen, Adv. Sci. 9 (20) (2022) 2106071, https://doi.org/10.1002/advs.202106071.

[31] Y. Liu, H.J. Busscher, B. Zhao, Y. Li, Z. Zhang, H.C. van der Mei, Y. Ren, L. Shi, Surface-adaptive, antimicrobially loaded, micellar nanocarriers with enhanced penetration and killing efficiency in staphylococcal biofilms, ACS Nano 10 (4) (2016) 4779–4789, https://doi.org/10.1021/acsnano.6b01370.

[32] S. Felz, P. Vermeulen, M.C.M. van Loosdrecht, Y.M. Lin, Chemical characterization methods for the analysis of structural extracellular polymeric substances (EPS), Water Res. 157 (2019) 201–208, https://doi.org/10.1016/j.watres.2019.03.068.

[33] Y. Wang, Z. Xu, W. Li, W. Wei, M. Qin, Q. Li, X. Liu, X. Zhang, X. Wang, A graphene-Ag based near-infrared defined accurate anti-scarring strategy for ocular glaucoma surgery, Biomater. Sci. 10 (5) (2022) 1281–1291, https://doi.org/10.1039/d1bm01614h.

[34] Q. Li, J. Liu, Y. Xu, H. Liu, J. Zhang, Y. Wang, Y. Sun, M. Zhao, L. Liao, X. Wang, Fast cross-linked hydrogel as a green light-activated photocatalyst for localized biofilm disruption and brush-free tooth whitening, ACS Appl. Mater. Interfaces 14 (25) (2022) 28427–28438, https://doi.org/10.1021/acsami.2c00887.

[35] Y. Huang, A.M. Vezeridis, J. Wang, Z. Wang, M. Thompson, R.F. Mattrey, N. C. Gianneschi, Polymer-stabilized perfluorobutane nanodroplets for ultrasound imaging agents, J. Am. Chem. Soc. 139 (1) (2017) 15–18, https://doi.org/10.1021/jacs.6b08800.

[36] J. Cen, X. Ye, X. Liu, W. Pan, L. Zhang, G. Zhang, N. He, A. Shen, J. Hu, S. Liu, Fluorinated copolypeptide-stabilized microbubbles with maleimide-decorated surfaces as long-term ultrasound contrast agents, Angew. Chem., Int. Ed. Engl. 61 (41) (2022) 202209610, https://doi.org/10.1002/anie.202209610.

[37] Y. Wang, Q. Liao, J. Chen, W. Huang, X. Zhuang, Y. Tang, B. Li, X. Yao, X. Feng, X. Zhang, M. Su, Z. He, T.J. Marks, A. Facchetti, X. Guo, Teaching an old anchoring group new tricks: enabling low-cost, eco-friendly hole-transporting materials for efficient and stable perovskite solar cells, J. Am. Chem. Soc. 142 (39) (2020) 16632–16643, https://doi.org/10.1021/jacs.0c06373.

[38] G. Qi, F. HuKenry, K.C. Chong, M. Wu, Y.H. Gan, B. Liu, Bacterium-templated polymer for self-selective ablation of multidrug-resistant bacteria, Adv. Funct. Mater. 30 (31) (2020) 2001338, https://doi.org/10.1002/adfm.202001338.

[39] J.A. Lemos, S.R. Palmer, L. Zeng, Z.T. Wen, J.K. Kajfasz, I.A. Freires, J. Abranches, L.J. Brady, The Biology of Streptococcus mutans, Microbiol. Spectr. 7 (1) (2019) GPP3, https://doi.org/10.1128/microbiolspec.GPP3-0051-2018, 0051-2018.
[40] S. Bolte, F.P. Cordelieres, A guided tour into subcellular colocalization analysis in light microscopy, J. Microsc. 224 (Pt 3) (2006) 213–232, https://doi.org/10.1111/j.1365-2818.2006.01706.x.
[41] P. Parvekar, J. Palaskar, S. Metgud, R. Maria, S. Dutta, The minimum inhibitory concentration (MIC) and minimum bactericidal concentration (MBC) of silver nanoparticles against Staphylococcus aureus, Biomater. Invest. Dent. 7 (1) (2020) 105–109, https://doi.org/10.1080/26415275.2020.1796674.
[42] B. Cao, F. Xiao, D. Xing, X. Hu, Polyprodrug antimicrobials: remarkable membrane damage and concurrent drug release to combat antibiotic resistance of methicillin-resistant Staphylococcus aureus, Small 14 (41) (2018) 1802008, https://doi.org/10.1002/smll.201802008.
[43] Y. Li, F. Liu, J. Zhang, X. Liu, P. Xiao, H. Bai, S. Chen, D. Wang, S.H.P. Sung, R.T. K. Kwok, J. Shen, K. Zhu, B.Z. Tang, Efficient killing of multidrug-resistant internalized bacteria by AIEgens in vivo, Adv. Sci. 8 (9) (2021) 2001750, https://doi.org/10.1002/advs.202001750.
[44] W. Wang, Y. Zhang, Z. Wang, X. Liu, S. Lu, X. Hu, A native drug-free macromolecular therapeutic to trigger mutual reinforcing of endoplasmic reticulum stress and mitochondrial dysfunction for cancer treatment, ACS Nano 17 (11) (2023) 11023–11038, https://doi.org/10.1021/acsnano.3c03450.
[45] D.H. Kim, J. Bae, J.H. Heo, C.H. Park, E.B. Kim, J.H. Lee, Nanoparticles as next-generation tooth-whitening agents: progress and perspectives, ACS Nano 16 (7) (2022) 10042–10065, https://doi.org/10.1021/acsnano.2c01412.
[46] A. Kikly, S. Jaafoura, S. Sahtout, Vital laser-activated teeth bleaching and postoperative sensitivity: a systematic review, J. Esthetic Restor. Dent. 31 (5) (2019) 441–450, https://doi.org/10.1111/jerd.12482.
[47] X.C. Shi, H. Ma, J.L. Zhou, W. Li, The effect of cold-light-activated bleaching treatment on enamel surfaces in vitro, Int. J. Oral Sci. 4 (4) (2012) 208–213, https://doi.org/10.1038/ijos.2012.70.